JGR Solid Earth

RESEARCH ARTICLE
10.1029/2021JB021803

Post-2018 Caldera Collapse Re-Inflation Uniquely Constrains Kīlauea's Magmatic System

Taiyi Wang[1], Yujie Zheng[2], Fabio Pulvirenti[3], and Paul Segall[1]

[1]Department of Geophysics, Stanford University, Standford, CA, USA, [2]Division of Geological and Planetary Sciences, California Institute of Technology, Pasadena, CA, USA, [3]Nanjing University of Information Science and Technology, Nanjing, China

Key Points:

- Simultaneous summit inflation and deflation constrain the location and geometry of Halema'uma'u (HMM) and South Caldera (SC) reservoirs
- A model with time dependent magma flux between reservoirs explains the post-collapse spatial-temporal deformation pattern
- Time dependent deformations require a HMM-East Rift Zone (ERZ) pathway and a significantly less hydraulically conductive SC-ERZ pathway

Supporting Information:

Supporting Information may be found in the online version of this article.

Correspondence to:

T. Wang,
taiyi@stanford.edu

Citation:

Wang, T., Zheng, Y., Pulvirenti, F., & Segall, P. (2021). Post-2018 caldera collapse re-inflation uniquely constrains Kīlauea's magmatic system. *Journal of Geophysical Research: Solid Earth*, *126*, e2021JB021803. https://doi.org/10.1029/2021JB021803

Received 29 JAN 2021
Accepted 17 MAY 2021

Abstract From August 2018 to May 2019, Kīlauea's summit exhibited unique, simultaneous, inflation and deflation, apparent in both GPS time series and cumulative InSAR displacement maps. This deformation pattern provides clear evidence that the Halema'uma'u (HMM) and South Caldera (SC) reservoirs are distinct. Post-collapse inflation of the East Rift Zone (ERZ), as captured by InSAR, indicates concurrent magma transfer from the summit reservoirs to the ERZ. We present a physics-based model that couples pressure-driven flow between these magma reservoirs to simulate time dependent summit deformation. We take a two-step approach to quantitatively constrain Kīlauea's magmatic plumbing system. First, we jointly invert the InSAR displacement maps and GPS offsets for the location and geometry of the summit reservoirs, approximated as spheroidal chambers. We find that HMM reservoir has an aspect ratio of ~1.8 (prolate) and a depth of ~2.2 km (below surface). The SC reservoir has an aspect ratio of ~0.14 (oblate) and a depth of ~3.6 km. Second, we utilize the flux model to invert GPS time series from 8 summit stations. Results favor a shallow HMM-ERZ pathway an order of magnitude more hydraulically conductive than the deep SC-ERZ pathway. Further analysis shows that the HMM-ERZ pathway is required to explain the deformation time series. Given high-quality geodetic data, such an approach promises to quantify the connectivity of magmatic pathways between reservoirs in other similar volcanic systems.

1. Introduction

The supply, storage, and subsurface transport of magma are some of the most fundamental, yet least understood volcanic processes (Poland et al., 2014). These processes, along with eruptive dynamics, are modulated by the geometry and nature of the pathways connecting magmatic reservoirs (Keating et al., 2008). The geometry and dimensions of individual pathways can be constrained by inverting surface deformation with continuum mechanics based models (e.g., Owen et al., 2000; Montagna & Gonnermann, 2013). However, with multiple reservoirs and a network of magmatic pathways, estimating the dimensions of each pathway directly from deformation can be challenging. Because magma flux is proportional to the hydraulic conductivity of the pathway, and pressure change in a reservoir depends on magma flux, time dependent deformation associated with each reservoir may reveal the connectivity of a multi-reservoir system (e.g., Bato et al., 2018; Le Mével et al., 2016; Reverso et al., 2014). Here we demonstrate that, physics-based models, coupled with Bayesian inversion, can synthesize multi-reservoir conceptual models with geodetic measurements to quantitatively constrain the hydraulic connectivity of magmatic systems.

Despite decades of research, the nature of Kīlauea's summit reservoirs and their connectivity to the East Rift Zone remains enigmatic (we reserve "East Rift Zone" for the geographic location and "ERZ" for the reservoir active in the observation period). Efforts to interpret summit deformation in terms of simple reservoir models yielded diverse reservoir locations and geometries (e.g., Baker & Amelung, 2012; Fiske & Kinoshita, 1969). Although modeled reservoirs cluster into two groups - a shallow Halema'uma'u (HMM) and a deeper South Caldera (SC) reservoir (e.g., Cervelli & Miklius, 2003; Poland et al., 2014), it has been suggested that the summit system represents a single irregularly shaped reservoir (Dieterich & Decker, 1975; Ryan, 1988). This ambiguity arises because deformation signals associated with these reservoirs are almost always of the same sign. The configuration of magmatic pathways connecting Kīlauea's summit reservoirs and ERZ is also elusive. Cervelli and Miklius (2003) argue that an "Γ shaped" pathway connecting the deeper SC reservoir to the shallower HMM reservoir, and then to ERZ, is required to explain the drainage

of magma from HMM during the deflationary stage of Deflation-Inflation (DI) events. Poland et al. (2014) suggest that ERZ is connected to the summit directly via SC, informed by depths of seismicity associated with dike intrusions in the East Rift Zone. Therefore, a robust constraint on the location and geometry of the summit reservoirs, as well as quantitative estimates on the conductivity of magma pathways, address these unresolved questions.

The largest caldera collapse at Kīlauea in at least 200 years, the 2018 event provides a rich data set to investigate its magmatic plumbing system (Anderson et al., 2019; Neal et al., 2019; Tepp et al., 2020). After the collapse of the Pu'u 'Ō'ō vent on April 30, a down-rift intrusion resulted in 3 months of fissure eruptions in the Lower East Rift Zone (LERZ) and 62 discrete collapse events in the summit. Flow volume estimates indicate up to 1.4 km^3 dense rock equivalent of magma was erupted from the LERZ over the period (Dietterich et al., 2021), a rate orders of magnitude higher than the estimated average magma supply from mantle, 0.06–0.18 km^3/yr (Dzurisin & Poland, 2018). The high eruption rate resulted in substantial pressure perturbations within Kīlauea's summit magma system, which would be expected to result in a period of post eruption inflation.

We report here on post caldera collapse simultaneous inflationary and deflationary deformation northwest and southeast of the caldera, respectively (Figures 1c and 1d). During this period, there was concurrent inflationary deformation in the mid-East Rift Zone near Pu'u 'Ō'ō (Figures 1a and 1b, e, f). These observations suggest a volume increase in the inferred HMM reservoir, a volume decrease in the inferred SC reservoir, and a volume increase in the ERZ. Global Positioning System (GPS) stations in the summit region registered continued deflation (Figure 2c) after the eruption ended in August 2018. By November 2018, GPS stations on the northwestern side of the caldera (e.g., UWEV) started to register inflation, while stations on the southeastern side of the caldera (e.g., PUHI) experienced continued deflation. By mid-May 2019, all of the GPS stations in the summit area exhibited a gradual inflationary signal. The delayed inflation from the southeastern side of the caldera suggests that the SC reservoir supplied magma to the ERZ and/or HMM. Modeling the spatial-temporal summit deformation could lead to quantitative constraints not only on the location and geometry of the summit reservoirs, but also the conductivity of magmatic pathways between the summit magma system and the ERZ.

We present our findings in the following order: in Section 2, we introduce the relevant GPS and Interferometric Synthetic Aperture Radar (InSAR) data sets. Details on time series analyses and covariance matrices can be found in appendices A and B. We then perform a "static" inversion, where GPS offsets and InSAR Line of Sight (LoS) cumulative displacement maps are used to estimate the location and geometry of the HMM and SC reservoirs (Section 3). Because approximate, semi-analytical, spheroidal source models are used in this inversion, we examine their accuracy by comparing predicted surface deformation with that of a 3D finite element model, given the same set of model parameters. In addition, we perform an inversion with the finite element model to ensure that the estimated parameters are not biased by limitations of the semi-analytical models. In Section 3, we also estimate the aspect ratio and depth of the ERZ reservoir by inverting InSAR LoS displacements. In Section 4, we introduce a model to relate flux-controlled reservoir pressure with time dependent surface deformation. Finally, we perform a "dynamic" inversion using GPS time series to estimate the effective hydraulic conductivity of various pathways in magmatic plumbing system. In Section 6, we discuss the implications of the inversion results.

2. Geodetic Data

2.1. Global Positioning System (GPS)

Three-component, daily GPS solutions were retrieved for the period between August 9, 2018 and December 1, 2019 from 8 USGS operated GPS stations at Kīlauea's summit (Figures 2a and 2b). GPS processing techniques are described in Miklius et al. (2005). We do not correct for south flank motion or deformation of Mauna Loa. In the vicinity of the caldera, long term south flank motion is relatively small (<2 cm/yr in the horizontal component at AHUP (Poland et al., 2017)) compared to the summit deformation signals (~10 cm/yr). Inflationary deformation associated with Mauna Loa at Kīlauea summit is also judged to have been small during the study period. Detailed discussion of the noise covariance matrix of GPS time series data can be found in Appendix A.

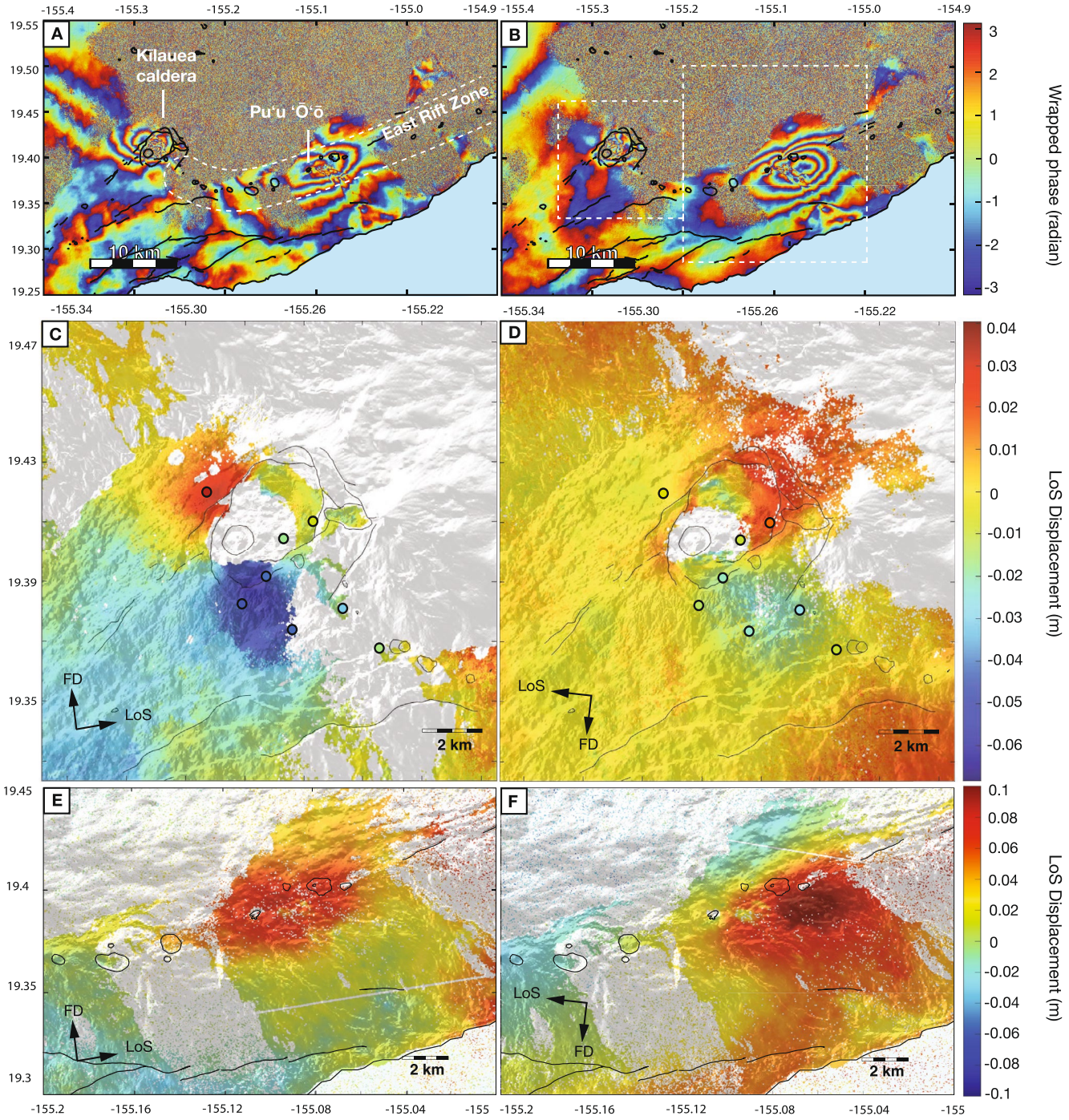

Figure 1. Post-collapse simultaneous inflation and deflation at Kīlauea summit and inflation in the East Rift Zone. (a), (b): ascending (November 22, 2018–May 27, 2019) and descending (November 13, 2018–May 30, 2019) wrapped interferograms of the summit region and the East Rift Zone. Each color cycle (red-yellow-blue) corresponds to 28 mm of displacement toward the satellite. Dashed boxes in (b) centered on Kīlauea summit and Pu'u 'Ō'ō correspond to displacement maps in (c)–(d), and (e)–(f), respectively. (c), (d): Small Baseline Subset (SBAS) derived ascending (November 4, 2018–March 16, 2019) and descending (November 1, 2018–March 19, 2019) cumulative displacement maps, respectively. Filled circles correspond to GPS station locations, with color indicating Line of Sight (LoS) projected GPS displacements. Areas with low coherence or large phase unwrapping errors are masked out. Color bar indicates range change in meters, with positive numbers indicating decreasing distance between satellite and ground. Black lines overlying the DEM demarcate the outline of the caldera prior to the 2018 collapse. (e), (f): ascending (November 4, 2018–March 16, 2019) and descending (November 1, 2018–March 19, 2019) LoS displacements of the East Rift Zone derived from interferograms.

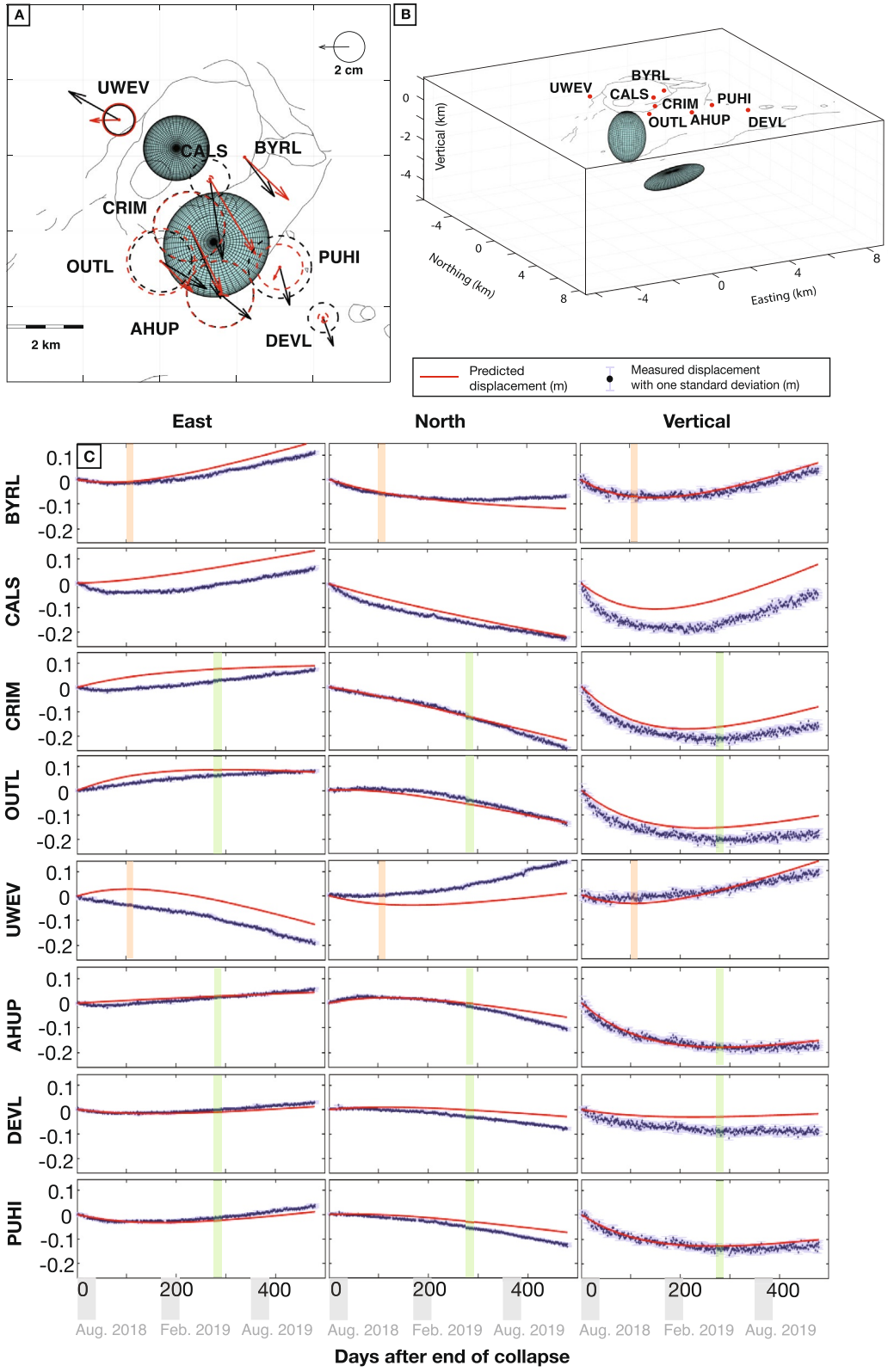
A
2 cm
UWEV
CALS
BYRL
CRIM
OUTL
PUHI
AHUP
DEVL
2 km
B
BYRL
UWEV
CALS
CRIM
PUHI
OUTL
AHUP
DEVL
Vertical (km)
Northing (km)
Easting (km)
Predicted displacement (m)
Measured displacement with one standard deviation (m)
East
North
Vertical
C
BYRL
CALS
CRIM
OUTL
UWEV
AHUP
DEVL
PUHI
0.1
0
-0.1
-0.2
0
200
400
Aug. 2018
Feb. 2019
Aug. 2019
Days after end of collapse

Figure 2

2.2. Interferometric Synthetic Aperture Radar (InSAR)

We utilize InSAR data to gain better spatial constraints on post-collapse deformation. For the summit area, we retrieved 44 ascending (path 124, frame 55–60) and 48 descending (path 524–529, frame 76) Sentinel-1 scenes (August 6, 2018–May 27, 2019) from Alaska Satellite Facility's data repository. SAR images were produced in geocoded coordinates (Zebker, 2017; Zheng & Zebker, 2017). Quality of interferograms was tested by reversing the order of re-sampling (geocoding from radar to lat-lon coordinates) and interferometry (creating interferogram and time-series), which produced <2 mm difference in standard deviation. To increase the signal-to-noise ratio, we perform a Small Baseline Subset (SBAS) time series analysis (Berardino et al., 2002). The SBAS derived time series displacements (Figure S1) for each pixel is used to compute cumulative displacement maps in the Line of Sight (LoS) directions (Figures 1c and 1d). Detailed procedures on SBAS and noise covariance matrices are presented in Appendix B. For the ERZ, we formed two interferograms with a pair of ascending acquisitions (November 4, 2018–March 16, 2019) and a pair of descending acquisitions (November 1, 2018–March 19, 2019) from Sentinel-1.

3. Static Inversion for the Geometry and Location of Reservoirs

3.1. Summit Reservoirs

3.1.1. Bayesian Inversion Using the Yang-Cervelli Model

We use GPS offsets and SBAS derived cumulative displacement maps to estimate the parameters that describe the HMM and SC reservoirs' centroid location, depth, aspect ratio, and orientation. A semi-analytical, approximate model originally proposed by Yang et al. (1988) to compute surface displacements due to a pressurized prolate spheroidal cavity in a homogeneous half space, later extended by Cervelli (2013) to include oblate cavities, is used to relate pressure change to surface displacements. We refer to this as the Yang-Cervelli model. The assumption of a homogeneous elastic half space is further discussed in Appendix C.

We first invert the cumulative displacements and thus refer to it as the "static inversion". We employ a Bayesian framework to estimate the posterior probability density function (PDF) of the model parameters:

$$P(\boldsymbol{m} \mid \boldsymbol{d}) \propto P(\boldsymbol{d} \mid \boldsymbol{m}) P(\boldsymbol{m}) \tag{1}$$

where $\boldsymbol{m}$ denotes model parameters and $\boldsymbol{d}$ the data. Equation 1 states that the probability of a model conditioned on data, $P(\boldsymbol{m}|\boldsymbol{d})$ (posterior), is proportional to the product of the likelihood, $P(\boldsymbol{d}|\boldsymbol{m})$, and the prior distribution of the model parameters, $P(\boldsymbol{m})$. In practice, the posterior PDF is estimated by a Markov Chain Monte Carlo (MCMC) procedure. We assume that the data errors are normally distributed, such that:

$$P(\boldsymbol{d} \mid \boldsymbol{m}) = (2\pi)^{-N/2} det(\boldsymbol{C})^{-1/2} \times exp\left[-\frac{1}{2}(\boldsymbol{d} - \boldsymbol{G}(\boldsymbol{m}))^T \boldsymbol{C}^{-1}(\boldsymbol{d} - \boldsymbol{G}(\boldsymbol{m}))\right] \tag{2}$$

Here, N is the total number of data points (GPS and InSAR), $\boldsymbol{C}$ is the data covariance matrix, $\boldsymbol{G}$ is the forward model operator. The accuracy of Equation 2 is predicated on having the correct covariance matrices for each data set. Three-component GPS offsets (Figure 1c) and SBAS-derived, quadtree down-sampled LoS cumulative displacement maps (Figures 4a and 4d) are used in the inversion.

To account for the disparity in the number of data points among GPS and InSAR data sets, we weighted the log likelihood of the GPS data by a factor of 1,000. This factor was obtained by inverting for the best-fit model with weight factors between 1 and 1,500, and computing the residual norms for both the GPS and

Figure 2. (a): Comparison of GPS offsets with predictions from the maximum a posteriori (MAP) model of the static inversion. Arrows and circles indicate radial and vertical displacements, respectively. Data is in black and predictions in red. Downward vertical displacement is indicated by dashed circles. Also included is the map view of the two best-fit spheroidal models from the static inversion. The spheroid to the northwest represents the Halema'uma'u (HMM) reservoir; the spheroid to the southeast represents the South Caldera (SC) reservoir. Note the volume of SC is assumed to be 2.5 km^3. (b): Perspective view of the best fit spheroidal magma chamber models. (c) Comparison of summit GPS time series with predictions from the MAP model of the dynamic inversion. Green and orange lines indicate the approximate dates when HMM and SC started to re-inflate, respectively. Error bars are ±1 standard deviation.

Table 1
Static Inversion Parameters, Bounds on Prior, MAP Model, and 90% Confidence Interval

Variable	Symbol	Unit	Bounds on the prior	MAP model	90% confidence interval
HMM E-W location	Δx_{HMM}	km	[0.3 0.5] [a]	0.46	[0.33 0.46]
HMM N-S location	Δy_{HMM}	km	[−0.5 0.5] [a]	0.35	[0.28 0.43]
HMM centroid depth	d_{HMM}	km	[−2.2 −1.5] [a]	−2.18	[−2.19 −2.12]
HMM aspect ratio	α_{HMM}	unit-less	[0.8 1.4] [a]	1.78	[1.68 1.79]
HMM pressure change	Δp_{HMM}	MPa	[1.5 2]	1.55	[1.52 1.63]
HMM volume	V_{HMM}	km^3	3.9 [b]	Fixed	
SC E-W location	Δx_{SC}	km	[−2.5 2.5] [c]	1.89	[1.75 1.97]
SC N-S location	Δy_{SC}	km	[−3.4 −1] [c]	−3.03	[−3.11 −2.88]
SC depth	d_{SC}	km	[−4.7 −2.7] [d]	−3.63	[−3.91 −3.48]
SC volume	V_{SC}	km^3	2.5 [e]	Fixed	
SC aspect ratio	α_{SC}	unit-less	[0.1 1]	0.14	[0.11 0.22]
SC pressure change	Δp_{SC}	MPa	[−1.99 −0.001]	−0.88	[−1.47 −0.70]
SC semi-major axis plunge	ϕ_{SC}	unit-less	[45 90]	63	[61 66]
SC semi-major axis trend	ψ_{SC}	unit-less	[0 360]	136	[127 142]

Horizontal locations are referenced to GPS station NPIT. The RMS misfit for the MAP model is 1.1 cm.
[a]Anderson et al., 2019; approximate posterior range. [b]Anderson et al., 2019; median estimate. [c]Poland et al., 2014; approximate locations of distributed sill opening. [d]Baker and Amelung, 2012; 95% confidence interval for the depth of "source 3." [e]Pietruszka and Garcia, 1999; magma mixing volume of SC inferred from residence time analysis.

InSAR data. With a weight factor of 1,000 (Figure S3), the prediction minimizes the L2 norm of covariance weighted residuals to each data set without compromising goodness-of-fit for either (Simons et al., 2002).

We assume Gaussian-tailed uniform distributions for the priors (Anderson & Poland, 2016), where the standard deviation of the tail is 10% the width of the uniform part. The choice of the prior, $P(\boldsymbol{m})$, is informed by previous studies at Kīlauea. We use the approximate range of Anderson et al. (2019)'s posterior distribution as priors for the horizontal location, depth, and aspect ratio for HMM (Table 1). Preliminary inversions indicate that prior constraints on the N-S location, depth, and aspect ratio of HMM may be overly restrictive for the post-collapse period. In particular, the inverted aspect ratio was consistently higher than the 95% upper bound of 1.4 found by Anderson et al. (2019). Due to the caldera collapse and the slumping of crustal material into the reservoir, it is plausible that the geometry of the hydraulically active part of the HMM reservoir evolved during the 2018 eruption. To allow for complete sampling of the model space, we extend the upper bounds on the N-S location, depth, and aspect ratio of HMM for the final inversion. We use previously inferred locations associated with SC as bounds on the prior (Baker & Amelung, 2012; Poland et al., 2014). The inferred SC volume generally falls between 2 and 20 km^3 (Poland et al., 2014). As expected, the goodness of fit is not sensitive to the volume of SC, due to trade-off between volume and pressure change. Here we use the estimated volume of 2.5 km^3 from Pietruszka and Garcia (1999) to compute the semi-major and -minor axes lengths of the SC reservoir.

Parameter PDFs are shown in Figure 3. For HMM, the best-fit value of Δx_{HMM} is well within its prior bounds. Δy_{HMM} is near its upper bound, which means the estimated centroid location of the HMM is further north than previous estimates. The best fit values of d_{HMM} and α_{HMM} are close to their respective upper bounds. To honor the prior constraints on d_{HMM} and α_{HMM} established by previous studies (e.g., Anderson et al., 2019), we do not further extend the bounds on these parameters. The posterior distributions of SC's parameters are well resolved within the prior bounds. The best-fit aspect ratio of SC is ~0.18, which is close to its lower bound and indicates a sill-like body. This is consistent with previous studies that modeled the SC reservoir as a penny-shaped crack (Baker & Amelung, 2012) or with distributed crack opening (Poland et al., 2014). Because the inversion allows SC to deviate from a vertical orientation, we observe that, in the maximum a posteriori (MAP) model, the semi-major axis plunges ~65° toward the SSW; the posterior PDF of the plunge excludes a vertical orientation of the reservoir. The dip is a result of fitting the imbalanced eastward

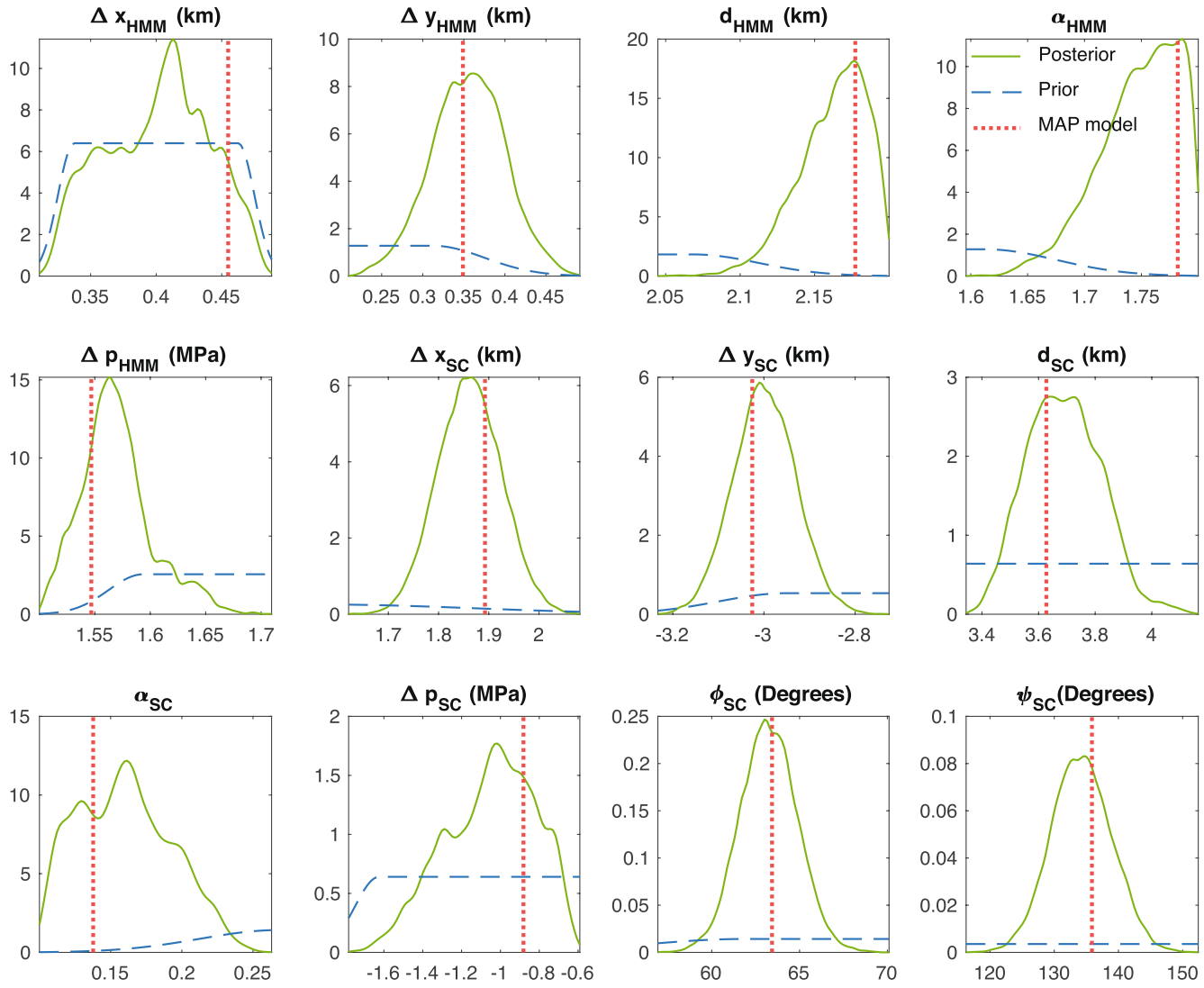

Figure 3. Posterior probability density functions (PDFs) from the static inversion (1×10^5 Markov Chain Monte Carlo [MCMC] iterations). Prior distributions are blue dashed lines; posterior distributions are in green; MAP model is in red dotted line. Δx, Δy: East-West and North-South coordinates relative to GPS station NPIT; d: depth relative to surface; α: aspect ratio; Δp: pressure change; ϕ, ψ: plunge and trend of the semi-major axis. Gaussian tailed uniform distributions are used as priors, where the standard deviation of the tail is one tenth the width of the uniform part. Note the inverted pressure changes are inversely correlated with prior constraints on reservoir volumes, as discussed in text.

and westward displacements associated with SC deflation (Figure 5). This feature is discussed further in Section 6.1.

The inflation northwest of the caldera and the deflation southeast of the caldera are captured by the prediction of the MAP model (Figure 4). The RMS misfit for the combined GPS and InSAR measurements is 1.1 cm. Notable misfits in GPS include the radial displacement at UWEV and the vertical displacement at CALS. Large misfit at UWEV may result from the asymmetry of the reservoir (Segall et al., 2020). Because CALS is situated on the 2018 collapse block, the assumption of homogeneous elastic half space may be violated (Figure 2a). The MAP model also under-predicts the ascending LoS range decrease and over-predicts the descending LoS range increase (Figure 4), which could result from geometrical simplicity of spheroidal source models. However, to ensure that the misfit is not due to boundary condition approximations inherent in the Yang-Cervelli model, we input the MAP model from the static inversion into a finite element (FEM) model to compute more accurate predictions of surface deformation.

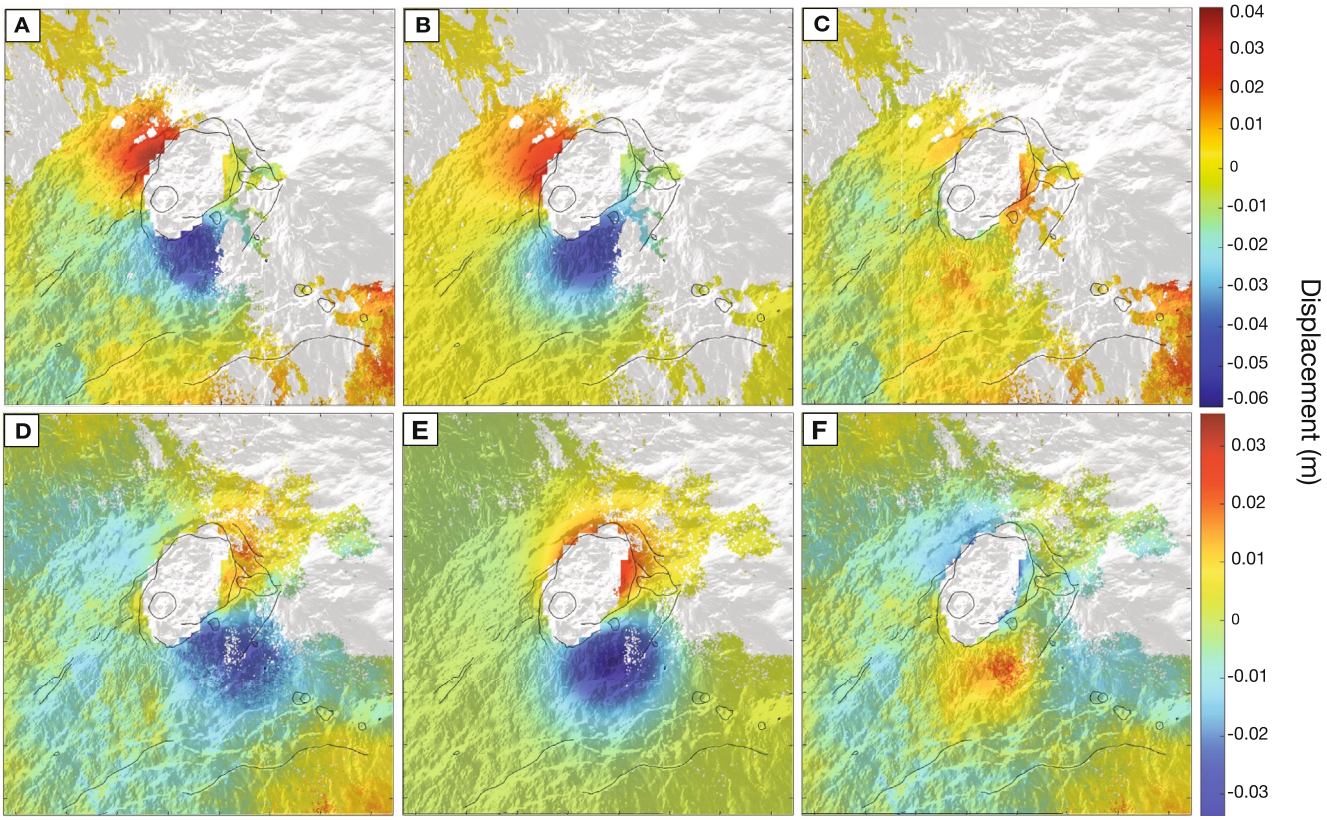

Figure 4. (a)–(c): Cumulative displacement derived from ascending track interferograms, prediction from MAP model of the static inversion, and residuals. (d)–(f): Cumulative displacement derived from descending track interferograms, prediction from MAP model of the static inversion, and residuals. The inflation to the northwest and deflation to the southeast are well captured by the prediction of the MAP model. Residuals in (f) are likely due to the geometric simplicity of the Yang-Cervelli model.

3.1.2. Comparison Against FEM Model Prediction

Given a homogeneous elastic half space, the accuracy of using the Yang-Cervelli model to predict surface deformation hinges on two conditions: 1. the depth to effective radius ratio of the spheroid cavity is large, so that the boundary conditions on the cavity/solid boundary (which ignores the free surface) are reasonably satisfied; 2. elastic interactions between the two cavities are negligible. To test the accuracy of the Yang-Cervelli model, we construct a FEM model in COMSOL based on the MAP model from the static inversion. Mesh sensitivity tests are performed to ensure the adequacy of the mesh resolution. We compare the observed east and vertical component displacements to the Yang-Cervelli predictions, and the FEM predictions (Figure 5). East and vertical component displacements are computed from the ascending and descending LoS cumulative displacement maps (Fialko et al., 2001). The north component of displacement is negligible because the near east-west SAR viewing angle is not sensitive to north-south displacements.

The Yang-Cervelli MAP model under-predicts the westward displacement west of HMM by more than 1 cm (Figure 5), whereas the FEM model under-predicts the westward displacement by a lesser degree. In the vertical component, the Yang-Cervelli model over-predicts the deflation to the southeast of the caldera, whereas the FEM model over-predicts both the inflation and the deflation. In both east and vertical components, the deformation pattern predicted by the FEM model is broader than predicted by the Yang-Cervelli model, which suggests that the depth of the HMM and SC reservoirs could be shallower than inferred from the Yang-Cervelli model. This raises the possibility that inversion with the FEM model could yield a more accurate location and geometry of the two reservoirs. In the next section, we demonstrate that inversion results from the Yang-Cervelli model are, in fact, not dissimilar to that from the more computationally expensive FEM model.

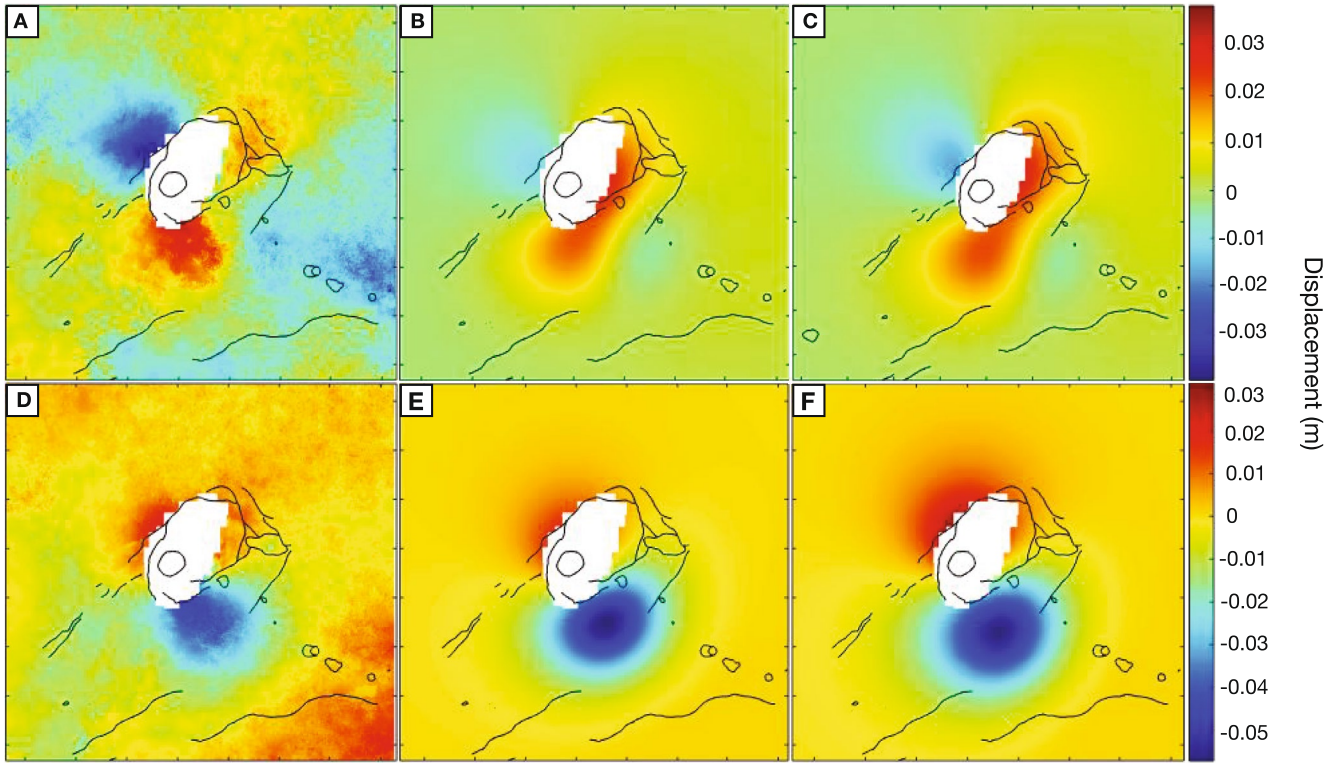

Figure 5. Comparison of SBAS derived cumulative displacement (between November 4, 2018 and March 16, 2019) with model predictions. (a)–(c): East component of measured deformation, prediction of MAP model, and prediction of MAP parameters as input into the FEM model, respectively. (d)–(e): vertical component of measured deformation, prediction of MAP model, and prediction of MAP parameters as input into the FEM model. Deformation within the caldera is masked due to potential unwrapping errors. The FEM predicted deformation pattern is broader than that from the MAP prediction and the data, indicating that the static inversion may overestimate the depths of both reservoirs.

3.1.3. Nelder Mead Inversion Using FEM Model

To test the accuracy of inversion results based on the Yang-Cervelli model, we perform an inversion with the FEM model and search within the $\sim\pm 2\sigma$ of the static inversion's posterior PDFs. We use the Nelder Mead method for the inversion. In doing so, we recognize that differences in inversion results could come from either the difference in inversion schemes (MCMC vs. Nelder Mead) or difference in forward model (Yang-Cervelli vs. FEM). In this section, we demonstrate that differences in inversion methods do not influence inversion results appreciably, and using the FEM model in lieu of the Yang-Cervelli model has a small effect on the inverted parameters.

Due to COMSOL's inability to include a non-diagonal covariance matrix, we opt to use a reduced data set for this inversion. The reduced data set is comprised of LoS displacements for 10 spatially separated InSAR pixel points (Figure S6) and 3-component GPS offsets during the same period. The 10 pixel points are chosen based on the rationale that the spatial correlation of atmospheric noise decreases exponentially with distance. For the same forward model and inversion scheme, the inverted model parameters are insensitive to full versus reduced data set (Table S1).

We use the MAP model from the static inversion (MCMC + Yang-Cervelli) as the starting model, and run the Nelder Mead + FEM inversion for 100 iterations, upon which the objective function converged to a constant value. The normalized difference between the best fit model parameters of the Nelder Mead inversion and the MAP model parameters is <10%. Because Nelder Mead is a downhill simplex algorithm, the inversion results may be sensitive to the initial model. To ensure that Nelder Mead inversion searched extensively over the model space, we perform a separate inversion using a generalized pattern search algorithm (Audet & Dennis, 2002) with the same bounds, and the Yang-Cervelli model. This inversion yields a best-fit model (Table 2) and a prediction (Figure 6) very similar to those obtained by Nelder Mead + FEM.

Table 2
Best Fit Models From Generalized Pattern Search + Yang Cervelli (RMS Misfit = 1.06 cm) and Nelder Mead + FEM (RMS Misfit = 1.10 cm)

Variable	Unit	Generalized pattern search + yang cervelli	Nelder Mead + FEM
Δx_{HMM}	km	0.56	0.36
Δy_{HMM}	km	0.47	0.27
d_{HMM}	km	−2.1	−2.2
α_{HMM}	unit-less	1.9	1.7
Δp_{HMM}	MPa	1.6	1.4
Δx_{SC}	km	1.8	1.5
Δy_{SC}	km	−2.9	−3.1
d_{SC}	km	−3.5	−3.6
α_{SC}	unit-less	0.16	0.14
Δp_{SC}	MPa	−1.4	−0.88
ϕ_{SC}	unit-less	121	116
ψ_{SC}	unit-less	−48	−32

Δx, Δy: East-West and North-South coordinates relative to GPS station NPIT; d: depth relative to surface; α: aspect ratio; Δp: pressure change; ϕ, ψ: plunge and trend of the semi-major axis. Note that, the small difference between the two best-fit models is not resolvable from data, supporting the use of Yang-Cervelli model for inversions.

The generalized pattern search algorithm has been demonstrated to be able to search over multiple local minima (Audet & Dennis, 2002). Therefore, the similarity between the model found by generalized pattern search + Yang-Cervelli and the model found by Nelder Mead + FEM demonstrates the robustness of the Nelder Mead inversion. The similarity of the inverted parameters from both Nelder Mead + FEM and generalized pattern search + Yang-Cervelli to those from the MAP model demonstrates that inversions using the approximate Yang-Cervelli model yields accurate results, as compared to those from the computationally expensive FEM model. This justifies our use of the Yang-Cervelli model for subsequent dynamic inversions (Section 5).

3.2. ERZ Reservoir

Inflationary deformation in the East Rift Zone provides important constraints on the geometry and depth of reservoir(s) in this region. In particular, the inverted depth range is used as prior information (Appendix D) for the dynamic inversion. Since the focus of this study is on summit deformation, we jointly invert the quadtree down-sampled ascending and descending interferograms of the East Rift Zone using surrogate optimization (Gutmann, 2001), instead of sampling the full PDFs using MCMC. A single Yang-Cervelli spheroid is used as the source model (crack-like model may also fit the data but was not attempted). We use the L2 norm of misfit weighed by spatial covariance matrices (obtained using the same method as detailed in Appendix B) as the objective function. The best fit model is a spheroid with an aspect ratio of 15.3, with a nearly horizontal semi-major axis striking sub-parallel to the East Rift Zone. The centroid is ∼2.3 km below the surface. The aspect ratio and centroid depths are not sensitive to the input reservoir volume. For a hypothetical volume of 2.5×10^9 m^3, the semi-major axis is ∼5,200 m, and the semi-minor axis is ∼340 m. The RMS misfit is 2 cm (See Fig. S5 for data-prediction-residual comparison).

4. Physics Based Magma Flux Model

Conceptual models of basaltic magma reservoirs typically involve an inner, molten region (liquid), a lower "mush" region (mixture of solid and liquid), and an elastic crust (solid) that bounds the reservoir. Flow between reservoirs can be through dikes, conduits, or porous media (Delaney & Gartner, 1997; Diez et al., 2005; Mastin & Ghiorso, 2000; Papale et al., 1998; Pollard & Delaney, 1978; Wilson & Head, 1981). We seek to model a multi-reservoir system by correctly representing the physics without overly complicating the model. In this study, we view the magma reservoirs as magma-filled cavities embedded in elastic crust. Although a simple representation of the complex system in nature, such an approach has been proven to be useful in geodetic modeling, if the time constants for stress relaxation are long compared to the time period under consideration (Appendix C). We use effective hydraulic conductivity to linearly relate pressure differences to magma flux and to parameterize the resistance to flow. We acknowledge that magmatic pathways can take the form of porous flow or conduits. The effective hydraulic conductivity provides a universal measure of how easily magma can flow through certain region under given pressure. For simplicity, we assume constant magma density in space and time.

To quantitatively assess the connectivity between the HMM, SC, and ERZ reservoirs, we propose a physics-based flux model in the form of a system of ordinary differential equations (ODEs). These ODEs describe the time evolution of both magma flux and reservoir pressure in a multi-reservoir system (Figure 7). We neglect momentum balance, which dictates the short-term dynamics of pressure variations within reservoirs. The volume flux between reservoirs is dictated by two fundamental relationships:

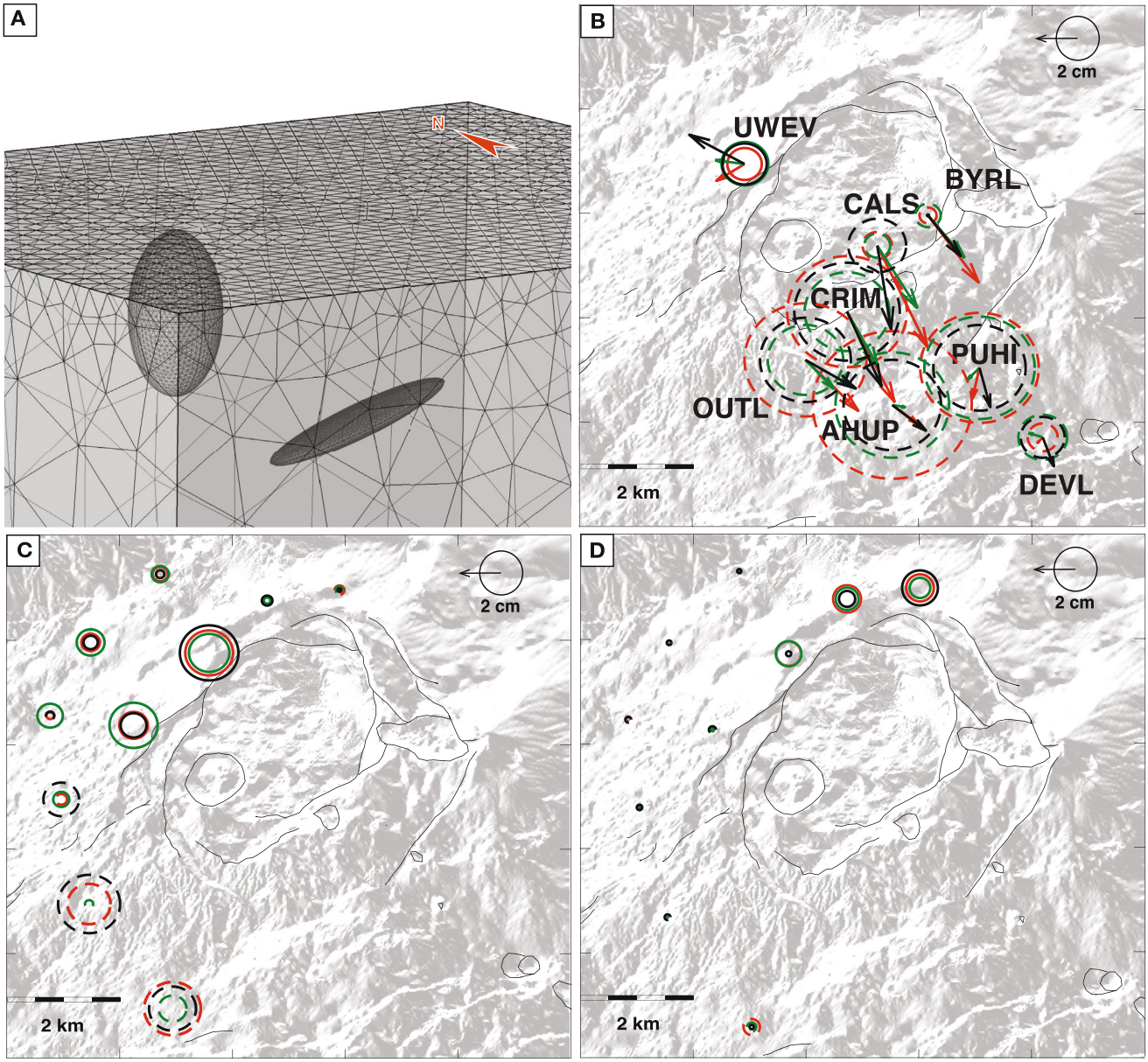

Figure 6. Nelder-Mead + FEM inversion results compared to generalized pattern search + Yang Cervelli inversion results. All displacements are computed for the period between November 4, 2018 and March 16, 2019. (a): mesh of the FEM model constructed in COMSOL. (b)–(d): Comparison of displacement data (black) with Nelder Mead + FEM best prediction (green) and Generalized Pattern Search + Yang-Cervelli best prediction (red). (b), (c), (d) are for GPS, ascending LoS, and descending LoS, respectively. All predictions are computed in the FEM model. The best-fit predictions from inversions using FEM versus Yang-Cervelli models are very similar, supporting the use of Yang-Cervelli model for inversions.

$$q = k\Delta p \tag{3a}$$

$$\frac{\partial p}{\partial t} = \frac{q}{V\beta} \tag{3b}$$

where k is the effective hydraulic conductivity, q is volumetric flux, p is reservoir pressure, Δp is the pressure difference between the two connected reservoirs, V is the magma chamber volume, and β the total compressibility (combined compressibility of the magma chamber and the magma therein) of the reservoir. Equation 4a states that magma flow rate is proportional to the pressure difference between the two magma

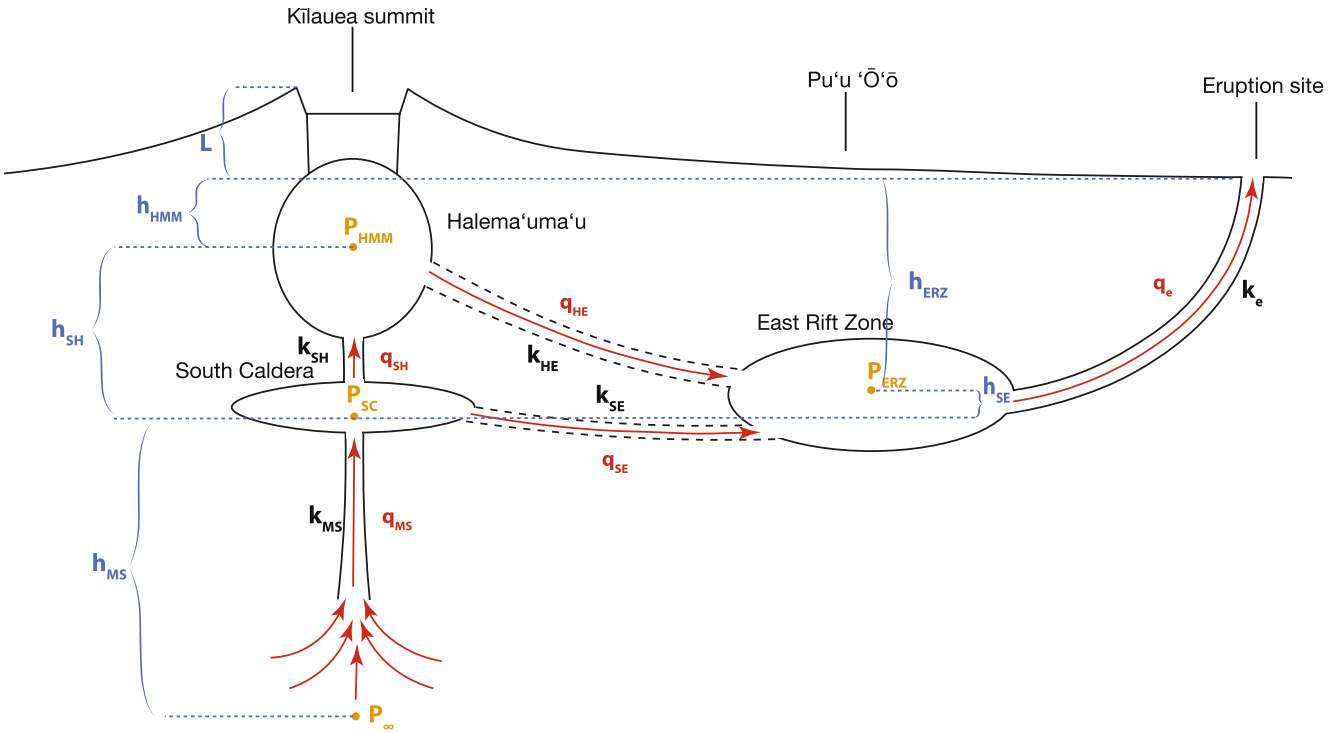

Figure 7. Schematic of the magma system model. p_{HMM}, p_{SC}, and p_{ERZ} indicate the pressure at the centroid of the HMM, the SC, and ERZ reservoirs. k indicates the effective hydraulic conductivity of pathways that connect magma reservoirs and the eruptions site. h indicates elevation difference between reservoirs. q indicates volume flux. L indicates the elevation difference between the summit and the eruption site, which is set to 1,000 m.

reservoirs and the pathway's effective hydraulic conductivity (Mastin et al., 2008). Spatially uniform pressure gradient along a magma pathway connecting reservoirs is assumed. Equation 4b (Segall et al., 2001) states that the rate of change of pressure inside a magma chamber varies as a function of total mass flux into the magma chamber, and is inversely proportional to both the volume and the total compressibility of the reservoir. This equation is derived from mass balance and assumed constant magma and chamber compressibility.

Our conceptual model accommodates both the "Γ shaped" (e.g., Cervelli & Miklius, 2003) and the "Y shaped" (e.g., Poland et al., 2014) configurations between HMM, SC, and the ERZ (Figure 7). By maximizing the number of potential magmatic pathways in the model, we allow the geodetic data to constrain the required pathways and associated hydraulic conductivity. We obtain the following expressions for volume flux through each pathway:

$$q_e = k_e(p_{ERZ} - \rho g h_{ERZ}) \tag{4a}$$

$$q_{HE} = k_{HE}(p_{HMM} - \rho g(h_{HMM} - h_{ERZ}) - p_{ERZ}) \tag{4b}$$

$$q_{SH} = k_{SH}(p_{SC} - p_{HMM} - \rho g h_{HS}) \tag{4c}$$

$$q_{SE} = k_{SE}(p_{SC} - \rho g h_{SE} - p_{ERZ}) \tag{4d}$$

$$q_{MS} = k_{MS}(p_\infty - p_{SC} - \rho g h_{MS}) = k_{MS}(p_{in} - p_{SC}) \tag{4e}$$

$$p_{in} = p_\infty - \rho g h_{MS} \tag{4f}$$

Table 3
Dynamic Inversion Parameters, Bounds on the Uniform Part of Prior Distributions, MAP Model, and 90% Confidence Interval

Variable	Symbol	Unit	Bounds on the prior	MAP model	90% confidence interval
HMM - ERZ conductivity	k_{HE}	$m^3\ s^{-1}\ Pa^{-1}$	$[10^{-10.2}\ 10^{-3.8}]$	$10^{-7.68}$	$[10^{-7.78}\ 10^{-7.30}]$
SC - HMM conductivity	k_{SH}	$m^3\ s^{-1}\ Pa^{-1}$	$[10^{-13.2}\ 10^{-6.8}]$	$10^{-7.95}$	$[10^{-8.14}\ 10^{-7.68}]$
SC - ERZ conductivity	k_{SE}	$m^3\ s^{-1}\ Pa^{-1}$	$[10^{-10.2}\ 10^{-3.8}]$	$10^{-8.98}$	$[10^{-9.66}\ 10^{-8.14}]$
Mantle - SC conductivity	k_{MS}	$m^3\ s^{-1}\ Pa^{-1}$	$[10^{-10.2}\ 10^{-3.8}]$	$10^{-6.82}$	$[10^{-6.94}\ 10^{-6.69}]$
HMM initial pressure	p^i_{HMM}	MPa	[11 35]	26	[20 30]
SC initial pressure	p^i_{SC}	MPa	[49 148]	130	[121 142]
ERZ initial pressure	p^i_{ERZ}	MPa	[41 123]	50	[46 70]
Mantle overpressure	p_{in}	MPa	[72 417]	130	[121 142]
HMM total compressibility	β_{HMM}	Pa^{-1}	$[10^{-9.6}\ 10^{-8.6}]$	$10^{-9.51}$	$[10^{-9.53}\ 10^{-9.22}]$
SC volume compressibility product	$V_{SC}\beta_{SC}$	$m^3\ Pa^{-1}$	[1.70 17.83]	1.94	[1.88 2.64]
ERZ volume compressibility product	$V_{ERZ}\beta_{ERZ}$	$m^3\ Pa^{-1}$	$[10^{-4.2}\ 7.5]$	0.44	[0.32 1.26]
ERZ centroid depth	h_{ERZ}	km	[1.4 4.6]	4.0	[3.7 4.4]

The choice of prior bounds are discussed in Appendix D.

where ρ is bulk magma density, h is height of the relevant magma column, and g is the gravitational acceleration. Variable definitions can be found in Table 3. We use two initial letters of the two reservoirs connected by a pathway as subscripts to denote flux and conductivity. Pressure is denoted by the acronym of associated reservoir. Superscript of i indicates initial condition. The depth differences between reservoirs are accounted for by including magma-static pressures. Note that the elevation at which magma enters/exits a reservoir does not influence the magma flux between reservoirs due to the magma static term. We assume atmospheric pressure at the eruption site. Next, mass balance for each reservoir combined with a linearized equation of state, leads to:

$$\frac{dp_{HMM}}{dt} = \frac{-q_{HE} + q_{SH}}{V_{HMM}\beta_{HMM}} \tag{5a}$$

$$\frac{dp_{SC}}{dt} = \frac{-q_{SH} - q_{SE} + q_{MS}}{V_{SC}\beta_{SC}} \tag{5b}$$

$$\frac{dp_{ERZ}}{dt} = \frac{-q_e + q_{HE} + q_{SE}}{V_{ERZ}\beta_{ERZ}} \tag{5c}$$

Consolidating the above equations yields the pressure rate within the HMM, SC, and ERZ reservoirs:

$$\frac{dp_{HMM}}{dt} = \frac{-(k_{HE} + k_{SH})p_{HMM} + k_{SH}p_{SC} + k_{HE}p_{ERZ} + \rho g(k_{HE}h_{HMM} - k_{HE}h_{ERZ} - k_{SH}h_{HS})}{V_{HMM}\beta_{HMM}} \tag{6a}$$

$$\frac{dp_{SC}}{dt} = \frac{k_{SH}p_{HMM} - (k_{SH} + k_{SE} + k_{MS})p_{SC} + k_{SE}p_{ERZ} + \rho g(k_{SH}h_{HS} + k_{SE}h_{SE}) + k_{MS}p_{in}}{V_{SC}\beta_{SC}} \tag{6b}$$

$$\frac{dp_{ERZ}}{dt} = \frac{k_{HE}p_{HMM} + k_{SE}p_{SC} - (k_e + k_{HE} + k_{SE})p_{ERZ} + \rho g(k_e h_{ERZ} - k_{HE}h_{HMM} + k_{HE}h_{ERZ} - k_{SE}h_{SE})}{V_{ERZ}\beta_{ERZ}} \tag{6c}$$

Equation 4 represents a system of three coupled, first order, inhomogeneous, linear ODEs. Analytical solutions in principle exist. However, given the number of coefficients involved, the eigen-values and eigen-vectors are overwhelmingly complex and the solution is not very insightful.

Given initial pressures inside HMM, SC, and ERZ reservoirs and values for the constants, the pressure evolution in the three reservoirs can be solved numerically. By convolving pressure histories deduced from the dynamical model with the displacements caused by unit pressure changes, based on the Yang-Cervelli model, we obtain predicted surface deformations as functions of time.

5. Dynamic Inversion for the Effective Hydraulic Conductivity of Pathways

We aim to estimate the pressure history, volume flux, and effective conductivity of various magmatic pathways (Figure 7) using post-collapse GPS time series at the summit. Here we explain the feasibility of constraining parameters of interest from time dependent surface displacements and the setup for the dynamic inversion.

The characteristic scales of the system constrain the dynamics of pressure evolution and the observed displacement time history. The dynamic inversion heavily weights the displacement rate, which scales with the pressure rate:

$$\frac{\partial u}{\partial t} \propto \frac{(1-\nu)V}{\mu}\frac{\partial p}{\partial t} \tag{7}$$

where ν is Poisson's ratio and μ the crustal shear modulus. Therefore, the characteristic time, t^*, and pressure, p^*, dictate the rate and magnitude of surface displacement, respectively. For a single chamber, single pathway system, the characteristic time is $t^* = V\beta/k$. In the multi-reservoir case (Equation 4), each reservoir has multiple characteristic time scales, each corresponding to one magmatic pathway that connects to that reservoir.

The characteristic pressure for a reservoir is the difference between its initial pressure and its equilibrium pressure, $p^* = p^e - p^i$. The equilibrium pressure of each reservoir is obtained by solving Equation 4 while setting the left hand side to zero:

$$p^e{}_{HMM} = p_{in} - \rho g h_{SH} \tag{8a}$$

$$p^e{}_{SC} = p_{in} \tag{8b}$$

$$p^e{}_{ERZ} = -\rho g h_{HS} + \rho g h_{ERZ} - \rho g h_{HMM} + p_{in} \tag{8c}$$

Therefore, the time dependent surface displacements depend on the characteristic quantities t^* and p^*. To constrain the model parameters such as k, $V\beta$, and h, we minimize the degrees of freedom by leveraging prior constraints on other parameters. The location, geometry, and orientation of the magma reservoirs are fixed to that of the MAP model from the static inversion. In addition, we fix the volume of HMM to 3.9 km^3 due to the unique constraint obtained by Anderson et al. (2019). Gaussian-tailed priors based on scaling arguments and empirical evidence are employed (Appendix D). The flux of each magmatic pathway is constrained to be non-negative, corresponding to the flow directions indicated in Figure 7.

In each MCMC iteration, the flux model is used to predict time dependent displacements at the GPS sites for a period of 480 days after the end of the eruption. Surrogate optimization (Gutmann, 2001) is used to search for a model close to the global minimum of the objective function. We then use this model as the starting point for the MCMC inversion. We do not model time dependent displacement in the East Rift Zone due to the lack of GPS coverage in the area. Results are presented for $\sim 3 \times 10^6$ iterations (Figure 8). In the MAP model, k_{HE}, k_{SH}, and k_{MS} are on the order of $10^{-7} - 10^{-8}$ $m^3\ s^{-1}\ Pa^{-1}$, while k_{SE} is on the order of 10^{-9} $m^3\ s^{-1}\ Pa^{-1}$.

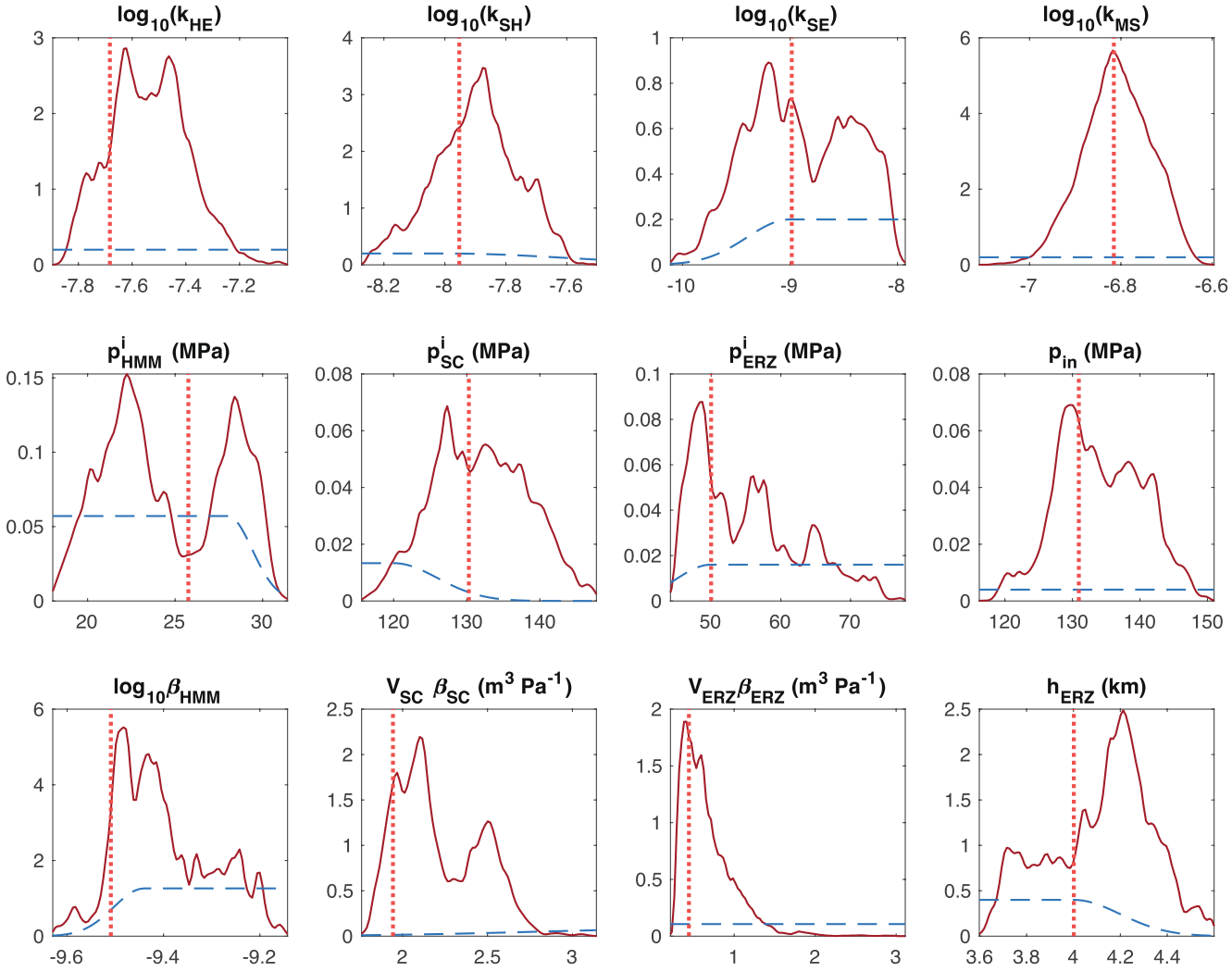

Figure 8. Posterior PDFs from the dynamic inversion (3×10^6 Markov Chain Monte Carlo [MCMC] iterations). Prior distributions are in blue dashed line; posterior distributions are in dark red; MAP model is in red dotted line. Gaussian tailed uniform distributions are used as priors, where the standard deviation of the tail is one tenth the width of the uniform part.

Approximately 80% of the variance in the time series data can be explained by the prediction of the MAP model (Figure 2). Notable deviations from the data exist in the east component of CALS, CRIM, and UWEV, the north component of UWEV, as well as the vertical component of CALS. We used the MAP model from the static inversion for the geometry, location, and orientation of the two summit reservoirs, which yielded relatively large residual in GPS offsets at some near-caldera stations (due to potentially inelastic effects at CALS and asymmetry of reservoir). Therefore, relatively large misfits in temporal deformation at these stations are not surprising (Figure 2).

6. Discussion

6.1. Location and Geometry of Reservoirs

The estimated east-west coordinates of HMM are in agreement with recent inversions from Anderson et al. (2019). However, our estimated location of HMM is farther north than previous estimates. The weak, positive correlation between the north-south coordinates of HMM and the west-east coordinates of SC may partially account for this discrepancy (Figure S4). The estimated centroid depth of HMM from the static inversion, 2.18 km below the surface, is consistent with previous geodetic estimates of 1–2 km below

the margin of the Halema'uma'u crater (Anderson et al., 2019; Lundgren et al., 2013; Montgomery-Brown et al., 2010; Poland et al., 2009). Our estimate is deeper than estimates of ∼1 km from seismic studies of the source of VLP tremor (Ohminato et al., 1998), VLP events (Almendros et al., 2002), and high resolution tomography (Dawson et al., 1999). The static inversion yielded a tightly constrained centroid depth for the SC reservoir. The MAP model indicates a centroid depth of ∼3.63 km, with a 90% confidence interval between 3.5 and 3.9 km below the surface (defined by the elevation of GPS station NPIT, 1,132 m above sea level). Decades of geodetic modeling constrained the depth of SC to be ∼3–4 km (Cervelli & Miklius, 2003; Dvorak et al., 1983; Eaton, 1962; Poland et al., 2014), the same depth range as an aseismic (Koyanagi et al., 1976) and low P-wave velocity zone (Ryan, 1988). As far as the authors are aware of, this is the best resolved depth of the SC reservoir. The estimated depths of HMM and SC are consistent with recent studies based on syn-eruptive melt inclusion entrapment pressures, which reveal a ∼2 km and a ∼3–5 km cluster believed to correspond to the HMM and SC reservoirs, respectively (Wieser et al., 2020).

The estimated geometry and orientation of the HMM and SC (Figure 3) reservoirs are required by specific features in the deformation data. Both vertical and horizontal components of the SBAS cumulative displacement maps exhibit opposite-signed displacements caused by the HMM and SC reservoirs (Figure 5). The magnitudes of the east-west displacements associated with HMM are comparable, indicating a relatively symmetrical and vertically oriented magma body. The large vertical to horizontal displacement ratio south of the caldera requires the SC reservoir to be oblate. The displacements south of the caldera exhibit larger eastward than westward displacements, which favors a northwest dipping SC reservoir.

The dynamic inversion yielded an ERZ reservoir centroid depth of 3.7–4.4 km below the surface (Figure 8), deeper than the 2.3 km inverted from InSAR LoS offset. The true centroid depth of ERZ is likely in between. The static inversion, based on kinematic modeling of InSAR data, is sensitive to the shallower, active part of the reservoir. The dynamic inversion, constrained by the time-dependent flux model, favors an ERZ deeper than the SC reservoir to maintain a favorable pressure gradient driving magma into the ERZ even when ERZ's pressure approaches that of the SC reservoir (Figure 9). The inferred centroid depth indicates that this ERZ reservoir is distinct from previously modeled shallow reservoirs in the East Rift Zone (Poland et al., 2014), and is consistent with the notion of a "deep rift zone" fed by downward draining of magma from the summit reservoirs (Ryan, 1988; Poland et al., 2014). Similar depths have been inferred from geodetic modeling of dike opening along the East Rift Zone (Owen et al., 2000). Our inferred ERZ reservoir depth is compatible with geochemical evidence that the Mg-rich olivine crystals were sourced from the deep rift zone during the 2018 LERZ eruption (Gansecki et al., 2019).

6.2. Hydraulic Connection Between Summit Reservoirs and ERZ

One of the central questions this study seeks to address is whether the ERZ is connected to the summit system via the HMM or SC reservoirs, or both. The two end member scenarios are of interest because the former indicates that magma supply at Kīlauea inevitably goes through the shallow HMM reservoir before flowing toward the ERZ. The later would suggest that magma can bypass the HMM reservoir before reaching the ERZ. The posterior PDFs indicate that, k_{SE} (SC-ERZ pathway) is more than an order of magnitude smaller than k_{HE} (HMM-ERZ pathway), k_{SH} (SC-HMM), and k_{MS} (mantle-SC).

6.2.1. Parameter Correlations

We investigate the correlations among the dynamic inversion parameters. Notably, a deeper ERZ reservoir tends to correlate with lower k_{HE} and k_{SE}, although the correlation is weak (Figure S8). This is because, for a higher magmastatic pressure within the ERZ, magma flux toward the ERZ is maintained by requiring the HMM-ERZ and SC-ERZ pathways to have lower conductivity. Larger $V_{ERZ}\beta_{ERZ}$ clearly leads to higher k_{HE}, k_{SH}, and k_{SE}. To decrease the magma flux leaving the summit over time, as deduced from GPS time series, pressure needs to increase in the ERZ. Larger $V_{ERZ}\beta_{ERZ}$ increases the flux required to increase the pressure within the ERZ, corresponding to higher k_{HE}, k_{SH}, and k_{SE}. Larger $V_{SC}\beta_{SC}$ tends to correlate with higher k_{HE}, k_{SH}, and k_{SE}. Lastly, higher k_{SE} weakly correlates with higher k_{HE}, suggesting that $k_{HE} \gg k_{SE}$ holds even for reasonably higher k_{SE}. These observations indicate that, despite the correlations among the dynamic

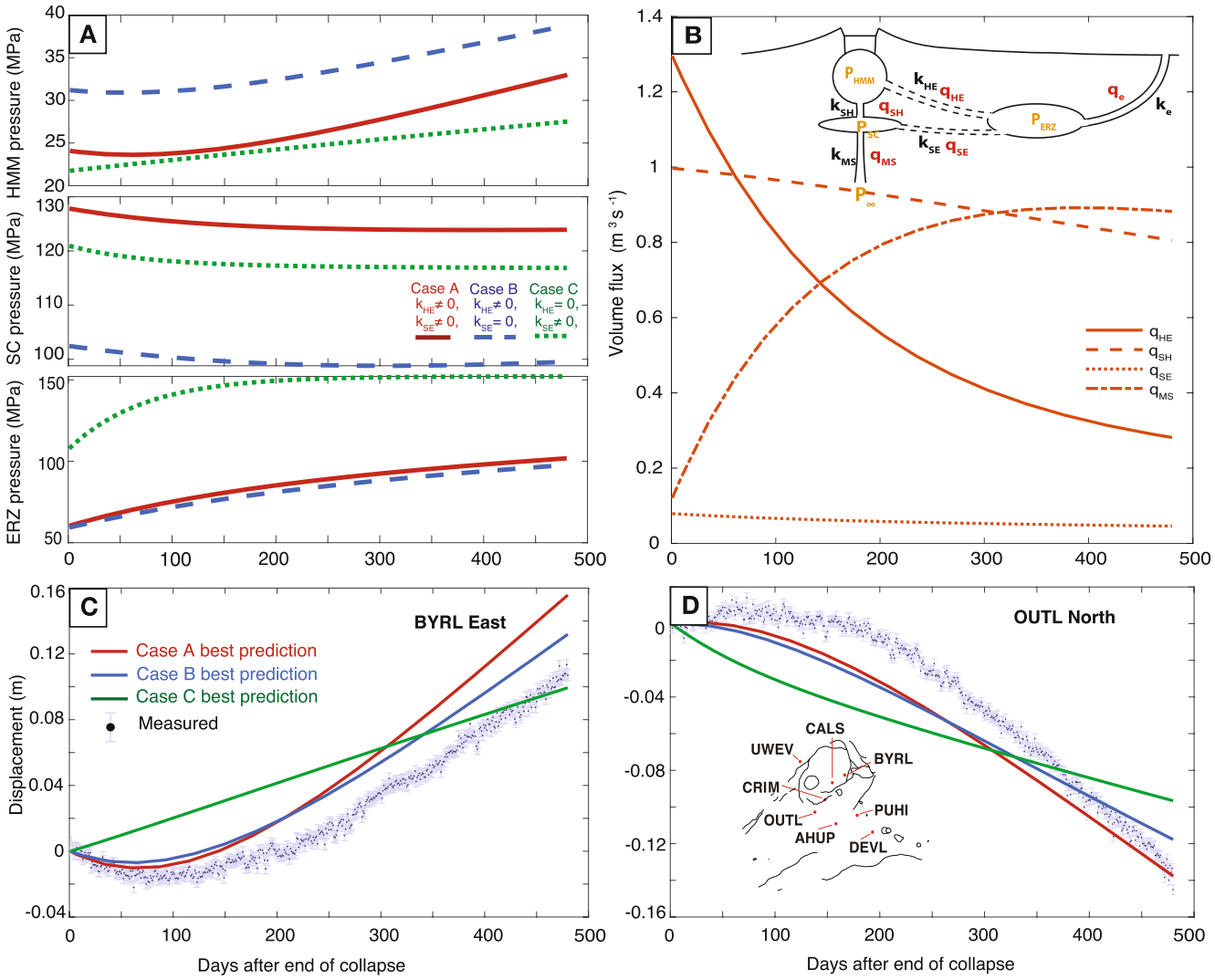

Figure 9. Pressure, volume flux and displacement comparisons. (a) Predicted pressure evolution within the Halema'uma'u (HMM), South Caldera (SC), and East Rift Zone (ERZ) reservoirs for three different cases. Case A (solid red): both HMM-ERZ and SC-ERZ are open. Case B (dashed blue): SC-ERZ is closed. Case C (dotted green): HMM-ERZ is closed. (b) Predicted volumetric fluxes over time. Inset shows the flux and effective conductivity pairs. (c), (d) Best-fit predictions from Case A, B, C versus GPS time series displacements for BYRL East and OUTL North, respectively. Without HMM-ERZ pathway, pressure inside HMM rises monotonically, producing monotonic displacements at GPS stations near HMM, contradicting observations.

inversion parameters, the conclusion that the HMM-ERZ pathway is much more conductive than the SC-ERZ pathway is robust.

6.2.2. End Member Cases

To better assess the two end member cases of summit - ERZ connections, HMM to ERZ only versus SC to ERZ only, we use MATLAB optimization algorithms (Audet & Dennis, 2002; Gutmann, 2001) to search for the bestfit models that satisfy each case (Figure 9). If the best prediction from one configuration cannot fit the data acceptably well, we reject that as a plausible configuration for the summit-ERZ connections. We search over the same model space (Table 3) as used in the dynamic inversion (Case A), except that in one case we close off the SC-ERZ pathway (Case B), and in the other we close off the HMM-ERZ pathway (Case C). When the SC-ERZ pathway is closed the curvatures of pressure history in all reservoirs have the same sign as those in the MAP model of Case A (Figure 9). However, when the HMM-ERZ pathway is closed, the curvature of the predicted HMM pressure history has the wrong sign compared to the data. In other

words, p_{HMM} from Case A decreases slightly before increasing (Figure 9), whereas p_{HMM} in Case C increases monotonically.

Because surface displacement is linear in pressure change, we do not expect the best prediction without a HMM-ERZ connection (Case C) to fit the displacements near HMM well. That is indeed the case. For example, at BYRL, the east component of GPS first moved west before moving east (Figure 9c). In the best-fit prediction for Case C, the east component moves monotonically eastward. OUTL first moved north, reversed direction and then accelerated to the south. The best-fit model under Case C, however, predicts decelerating southward displacement (Figure 9d), contradicting the data. The non-monotonic displacement trends in the radial components of BYRL and OUTL cannot be due to SC, which contributes very small radial displacements, as required by its oblate geometry.

Our observation that only Case A and B can fit the time varying displacements near HMM can be understood as follows: when the HMM-ERZ pathway is closed, HMM has a net influx of magma due to the higher overpressure in SC, resulting in monotonically increasing pressure within the HMM reservoir. Monotonic pressurization of HMM is not consistent with deformation time series. Therefore, the shallow connection between HMM and ERZ must exist. This is in agreement with Cervelli and Miklius (2003), who argued for a direct connection between HMM and the ERZ based on: 1. A shallower pathway is more likely to remain open when magma pressure inside the pathway is low; 2. without a shallow pathway between HMM and the ERZ, HMM's deflation during DI events implies magma draining back into the SC reservoir.

6.2.3. Possibility of HMM Draining Into SC

The prolonged and pronounced deflation at SC in the post-collapse period indicates a significant reduction in reservoir pressure for at least 300 days after the end of caldera collapse on August 4, 2018 (Figure 2). If HMM drained into SC immediately after the end of the collapse, the re-inflation of HMM (~100 days after the end of the collapse) would require an increase in SC pressure, contradicting the observations. To test whether magma could drain from HMM into SC immediately after the eruption we ran an optimization without forcing magma to flow from SC to HMM, keeping all pathways open. We found a best-fit model virtually the same as the MAP model, with magma flowing from SC to HMM. Therefore, it is not plausible that the deflation of HMM immediately after the cessation of the collapse events is associated with magma draining into the SC.

6.2.4. Comparison With Previous Studies

Previous estimates of the effective radius of an idealized circular conduit connecting HMM to Pu'u 'Ō'ō ranged from 1.7 to 2.5 m (Cervelli & Miklius, 2003; Patrick et al., 2015, 2019). Assuming the pathway connecting HMM and Pu'u 'Ō'ō vent is ~20 km long, the magma viscosity is 150 Pa · s, the MAP conductivity of the HMM-ERZ pathway translates to a radius of 0.63 m. If the ERZ is connected to the summit system through only HMM (Case B), the best-fit conductivity translates to an effective radius of 0.91 m. Both values are lower than previous estimates, although of the same order of magnitude. Caution needs to be taken in comparing effective radii with hydraulic conductivity of magma pathways during various periods, because magma viscosity is generally poorly constrained. In addition, trade-off between $V_{ERZ}\beta_{ERZ}$ and k_{HE} may at least partially account for the discrepancy with previous estimates.

A shallow HMM-ERZ pathway dominating magma supply to the ERZ in the post-collapse period is not inconsistent with recent findings by Wieser et al. (2020). They find that olivine crystals that grew at depths corresponding to HMM and SC were subsequently mixed into the erupted magmas. The scenario in which magma follows the SC-HMM-ERZ trajectory to produce mixed melt cannot be excluded based on their data (Wieser et al., 2020).

6.2.5. Summary

Although we cannot preclude that the ERZ is directly connected to SC from the available GPS time series, our analysis strongly suggests that the deeper SC-ERZ pathway is much more resistant to flow, at least during the post-collapse period (Figure 10). If connectivity in the co-collapse period is similar to that of the post-collapse period, the shallow connection between HMM and the East Rift Zone likely played a dominant role in supplying magma to the eruption site in 2018.

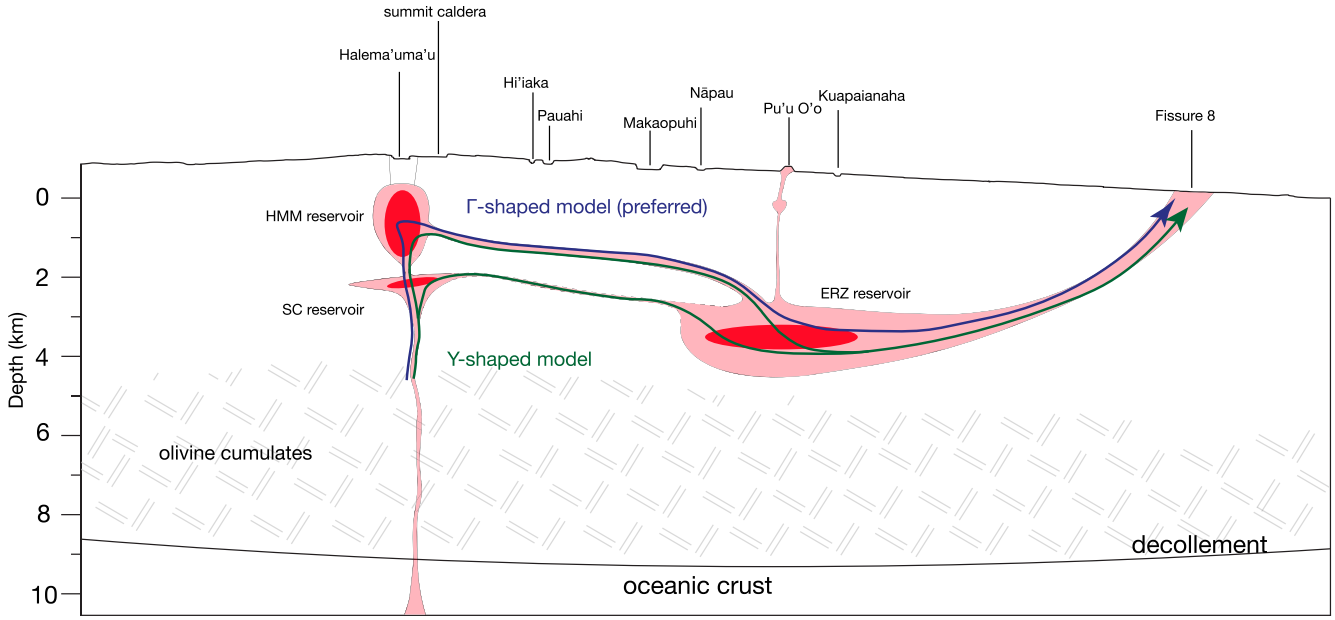

Figure 10. Schematic interpretation of the magmatic system that connects Kīlauea's summit reservoirs with the East Rift Zone and the 2018 Lower East Rift Zone eruption site (Fissure 8). Static inversion indicates that HMM reservoir is a vertically oriented, prolate spheroidal reservoir. The SC reservoir is approximated as an oblate spheroidal body tilting toward the northwest. The ERZ reservoir is a highly elongated body sub-parallel to the strike of the East Rift Zone. The dynamic inversion indicates that HMM-ERZ pathway is significantly more conductive than the SC-ERZ pathway. Overall, this study favors the Γ shaped connection from SC to HMM to the ERZ. While the geometry of the SC and ERZ reservoirs are relatively well constrained, their volumes are not. Depths to the centroid of reservoirs (red) are approximately to scale. Background geology adopted from Baker and Amelung (2015). Pink indicates the likely presence of mush outside of the hotter, fluid dominated core that geodetic data is sensitive to on short time scales.

6.3. Pressure and Magma Flux

The initial pressures in HMM, SC, and ERZ reservoirs are estimated to be 26, 130, and 50 MPa, respectively (Figure 8). The HMM initial pressure is consistent with the expected range based on pre- and co-collapse pressure loss (Appendix D). The SC initial pressure, p^i_{SC}, is at the higher end of the expected range, and could partially be explained by its positive correlation with mantle overpressure, p_{in}. As noted in Equation 5b, the characteristic pressure of the SC reservoir is the difference between the mantle overpressure and its initial pressure, resulting in a strong correlation between these quantities. The ERZ initial pressure, p^i_{ERZ}, is less than expected for an estimated ERZ reservoir depth of 4.0 km. This could result from trade-offs between the initial pressure in the ERZ and HMM, as seen in Equation 4b. If p_{HMM} and p_{ERZ} increase by the same amount, the flux between HMM and ERZ, q_{HE}, does not change. Furthermore, increasing p_{HMM} only changes q_{SH} slightly, because p_{SC} is much larger than p_{HMM}. Increasing p_{ERZ} will change the value of q_{SE}. However, because q_{SE} is small compared to other fluxes (k_{SE} is much smaller than either k_{HE}, k_{SH}, or k_{MS}), the overall dynamics of the system does not change significantly. We have verified through forward calculation that a higher p^i_{HMM} and p^i_{ERZ} can fit the data as well as the MAP model does.

The magma supply rates from SC to HMM and from the summit reservoirs to ERZ decrease monotonically (Figure 9b). Such trends are consistent with rising pressure inside HMM and ERZ, which lowers the driving pressure of magma flow into these two reservoirs. The increasing flux from the mantle, q_{MS}, results from a gradual decrease in pressure within the SC reservoir. Our estimated mantle flux reaches 0.9 $m^3\ s^{-1}$ toward the end of modeling period, below the 3.2–6.3 $m^3\ s^{-1}$ long-term supply rate at Kīlauea (Dzurisin & Poland, 2018). The underestimation of mantle supply rate may be due to the relatively poor resolution of mantle overpressure in the dynamic inversion. Higher mantle overpressure would result in higher mantle flux into the system.

7. Conclusions

Through analysis of GPS and InSAR data, we report unique post-collapse simultaneous inflation and deflation at Kīlauea's summit, as well as inflation in the East Rift Zone. We constrain the location and geometry of two distinct summit reservoirs via Bayesian inversion of cumulative GPS and InSAR derived displacements. We check the accuracy of the semi-analytical forward models using a fully three-dimensional (3D) finite element model of the two reservoirs. The centroid depths and geometry of the ERZ reservoir are estimated using similar methods. A physics-based flux model is devised to simulate the post-collapse, time-dependent deformation at Kīlauea's summit. By inverting the time series displacements with the flux model, we quantitatively constrain the effective conductivity of Kīlauea's various magmatic pathways. Our main findings are:

(1) Simultaneous inflation and deflation at Kīlauea's summit clearly indicates that HMM and SC are hydraulically distinct magma reservoirs, rather than different compartments of the same reservoir.
(2) Inversion of GPS and InSAR displacement offsets, assuming homogeneous half-space spheroidal magma chamber models, indicates that the centroid of the oblate SC reservoir is ∼3.6 km below surface, with a 90% confidence interval between 3.5 and 3.9 km.
(3) A multi-reservoir flux model (Figure 10) is proposed to explain the observed time dependent surface deformation. Constraints on the characteristic pressure and time from time dependent deformation lead to estimates of pathway hydraulic conductivity.
(4) A magmatic pathway between the HMM reservoir and the ERZ reservoir is required to explain the post 2018 caldera collapse GPS time series. The effective hydraulic conductivity of the inferred SC-ERZ pathway is an order of magnitude lower and could be zero.

Future work incorporating time dependent deformation from the pre-/co-collapse periods would enhance constraints on the hydraulic connectivity of the plumbing system and lend insight on whether these quantities evolve over time.

Appendix A: Estimating Covariance Matrices for GPS Noise

Estimating the amplitude of time dependent noise for GPS stations is challenging due to the persistent inflation-deflation cycles in the summit region. Assuming that random walk noise dominates time-dependent noise, we estimate the amplitude of white and random walk noise by fitting BYRL's vertical component time series with a third-order polynomial function. Optimization is done by maximizing the likelihood function (Equation 2) with a noise covariance that combines white and random walk noise. For the duration of the time series used in the dynamic inversion (480 days), the estimated random walk noise amplitude is consistently small ($< 1\text{mm} / \sqrt{\text{year}}$) compared to that of the white noise. Therefore, in the dynamic inversion we assume only white noise during the observation period. We also assume that the white noise amplitude for the same component of different summit GPS stations is the same, based on the fact that summit GPS stations have identical instrumentation and are located in a relatively small geographic region. The resulted white noise amplitude for east, north, and vertical component of GPS time series are: $\sigma_E = 0.0032$ m, $\sigma_N = 0.0027$ m, $\sigma_U = 0.0089$ m.

Appendix B: InSAR Time Series Analysis and Noise Covariance Matrices

To explain our workflow, we highlight the most essential components of the SBAS algorithm (Berardino et al., 2002). Consider M interferograms formed from N co-registered SAR images. On a pixel-by-pixel basis, we have a vector of N unknown phase values and a vector of M known phase differences:

$$\vec{\phi}^T = [\phi(t_1),\ldots,\phi(t_N)] \tag{B1a}$$

$$\delta\vec{\phi}^T = [\delta\phi_1,\ldots,\delta\phi_M] \tag{B1b}$$

To obtain a physically sound solution, Berardino et al. (2002) replace the unknowns with the mean phase velocity between adjacent time acquisitions, which has the form:

$$\vec{v} = \left[v_1 = \frac{\phi_1}{t_1 - t_0}, \ldots, v_N = \frac{\phi_N - \phi_{N-1}}{t_N - t_{N-1}} \right] \tag{B2}$$

where t_1,..., t_N are the acquisition times of the N SAR images, and t_0 the reference time when deformation is assumed to be 0. Therefore, the relationship between phase velocity and phase differences is:

$$\boldsymbol{B}\vec{v} = \delta\vec{\phi} \tag{B3}$$

$\boldsymbol{B}$ is a $M \times N$ matrix, the entries of which are the differences between acquisition times and 0's. The system is rank deficient and is inverted in the minimum-norm sense using the Moore-Penrose inverse.

B1. Phase Noise

The above formulation ignores phase noises in the data. In reality, the differential phase $\delta\vec{\phi}$ is the sum of at least the following differential phase components:

$$\delta\vec{\phi} = \delta\vec{\phi}_{topo} + \delta\vec{\phi}_{defo} + \delta\vec{\phi}_{tropo} + \delta\vec{\phi}_{orb} + \delta\vec{\phi}_{decorr} + \delta\vec{\phi}_{unwrap} + \delta\vec{\phi}_{iono} \tag{B4}$$

where $\delta\vec{\phi}_{topo}$ is the residual topographic differential phase; $\delta\vec{\phi}_{defo}$ is the phase difference attributed to surface displacement between acquisition times; $\delta\vec{\phi}_{tropo}$ is the differential phase due to the differences in propagation delay through the troposphere between SAR acquisitions; $\delta\vec{\phi}_{orb}$ is due to uncertainties in satellite orbits; $\delta\vec{\phi}_{decorr}$ represents the phase noise resulted from change in scattering properties of the resolution element over time; $\delta\vec{\phi}_{unwrap}$ is unwrapping error; $\delta\vec{\phi}_{iono}$ is introduced by dispersion in the ionosphere. Phase unwrapping errors are accounted for by masking the SBAS derived cumulative displacement maps based on the number of integer mis-closures, and specifically masking the caldera region for the purpose of inversion. Topographic phase is likely minor except inside the caldera, where the topographic relief is substantial and much of the signal is masked out. Sentinel 1 operates in C-band, which is minimally affected by ionospheric effects. In addition, ionospheric effects are usually at much longer wavelengths than the scale of our study area (Liang et al., 2019). Assuming orbital errors are small, temporal decorrelation and atmospheric delays are the major sources of noise in the differential phase.

B2. Temporal Covariance Matrix for Weighting SBAS

We employ SBAS to reduce decorrelation noise. Methods for propagating temporal decorrelation and atmospheric noise from individual interferograms to time series displacements have been developed (Agram & Simons, 2015), but incorporating the full spatial-temporal covariance matrix into SBAS remains computationally challenging. Given M interferograms formed from N SAR images, and each interferogram has P pixels, the total covariance matrix is of size $MP \times MP$. For computational tractability, we employ a standard pixel-by-pixel approach in our SBAS procedure. This approach is based on two assumptions: 1. both the atmospheric and temporal decorrelation phase noise are normally distributed with zero mean; 2. there is no spatial correlation between phase noises. Here, we treat the atmospheric phase as signal and the decorrelation phase as noise in the SBAS inversion, as reflected in the weighting scheme (Equation B7).

We use a temporal decorrelation covariance matrix, Σ_p^t, to weight the SBAS inversion (Guarnieri & Tebaldini, 2008; Tough et al., 1995). This weighting scheme favors pixel pairs with shorter temporal baselines and thus higher temporal correlation over temporally decorrelated pixel pairs. To get Σ_p^t, we first compute the coherence $\rho_{p,m}$ for each pixel p in interferogram m using the standard coherence estimator:

$$\rho_{p,m} = \frac{\sum_{x,y}^{k,l} s_{1x,y} s_{2x,y}^*}{\sqrt{\sum_{x,y}^{k,l} s_{1x,y} s_{1x,y}^* \sum_{x,y}^{k,l} s_{2x,y} s_{2x,y}^*}} \tag{B5}$$

where x, y are indices of the pixels over a $k \times l$ pixel region; s_1 and s_2 denote the complex values from two SAR acquisitions; superscript "$*$" indicates complex conjugate. The temporal decorrelation variance can then be related to the coherence by the following expression, in the limit of Cramer-Rao (16 looks in our case):

$$\sigma_{p,m}^2 = \frac{(1-\rho_{p,m}^2)}{2L\rho_{p,m}^2} \tag{B6}$$

where $\rho_{p,m}$ is the coherence of pixel p in interferogram m and L is the number of looks for each pixel. In keeping with common practice, we only use the diagonal form of Σ_p^t, $diag[\sigma_{p,1}^2,\sigma_{p,2}^2,\ldots,\sigma_{p,m}^2,\ldots,\sigma_{p,M}^2]$, to weight the SBAS inversion. We note that a more accurate form of temporal covariance model accounting for off-diagonal components has been recently proposed by Zheng et al. (2021). The more accurate form would result in higher uncertainty estimates for the SBAS time series, but would not change the static inversion results, as discussed in the next section. This is because only spatial covariance matrices were used to weight the inversion. Let $\boldsymbol{P} = (\Sigma_p^t)^{-1}$ be the weight matrix, we estimate a vector of average LoS velocity between the time of SAR acquisitions via:

$$\vec{v} = (\boldsymbol{B}^T\boldsymbol{P}\boldsymbol{B})^{-1}\boldsymbol{B}^T\boldsymbol{P}\overrightarrow{\delta\phi} \tag{B7}$$

by integrating $\vec{v}$ over time intervals between SAR acquisitions, we obtain the cumulative displacement over time $\vec{d}_p(t)$:

$$\vec{d}_p = \boldsymbol{\tau}\cdot\vec{v}_p \tag{B8a}$$

$$\boldsymbol{\tau} = \begin{bmatrix} \Delta t_{01} & 0 & \ldots & 0 \\ \Delta t_{01} & \Delta t_{12} & 0 & \vdots \\ \vdots & & \ddots & \vdots \\ \Delta t_{01} & \Delta t_{12} & \ldots & \Delta t_{N-1\,N} \end{bmatrix} \tag{B8b}$$

Differential phase measurements are defined relative to a spatial reference point and need to be calibrated. We choose the pixel co-located with GPS station CNPK as the reference point for the entire stack of interferograms. Post SBAS analysis, we calibrated the displacement time series of this pixel, so that $\vec{d}_{CNPK}$ is consistent with LOS projected GPS time series displacement from CNPK. A comparison between LoS-projected GPS and SBAS LoS displacements at co-located pixels (Figure S1) demonstrates the overall agreement between inverted SBAS time series displacement with GPS. To compute the average velocity for each pixel, we fit a liner model to the sub-period between November 4, 2018 and March 16, 2019 (day 88–220 in Figure S1), during which the temporal displacements are approximately linear in time. We then multiply the average deformation velocity by the duration of the sub-period (133 days) to obtain cumulative displacements for each pixel (Figure 1). This approach of computing cumulative displacement minimizes (temporally uncorrelated) decorrelation noise at each epoch.

B3. Spatial Covariance Matrix for Weighting Static Inversion

Two major sources of atmospheric phase delays are the stratified lower troposphere and turbulent mixing. Empirical methods evaluating phase dependence on elevation (e.g., Lin et al., 2010) and predictive methods based on Global Atmospheric Models (e.g., Jolivet et al., 2014) have been utilized to correct for stratified tropospheric delays. Unfortunately, empirical methods are difficult to implement due to the correlation of our signal with topography, whereas Global Atmospheric Models are not applicable in our case because their typical resolution (>30 km) is larger than our scenes. The summit region has relatively low topographic relief. Thus, we expect minimal error due to stratified atmosphere and do not correct for the associated delays. We compute the spatial covariance of turbulent atmospheric delay empirically and mitigate the effect of noise on the static inversion by weighting the data using the covariance.

We estimate the spatial covariance matrix, Σ_p^s ($p = 1,2,...,P$) by applying a semivariogram to the cumulative displacement map, similar to the application of a semivariogram to individual interferograms (Emardson et al., 2003; Lohman & Simons, 2005). This approach assumes that the noise is spatially isotropic: the covariance between two points separated by a scalar distance is only dependent on the distance, not on the location of these two points. The cumulative displacement map exhibits large signals due to deformation, which preclude direct sampling of this map to calculate the variance-covariance matrix. Therefore, we filter the cumulative displacement map with a high-pass Gaussian filter, the kernel of which is a 310 by 310 pixel square matrix with a standard deviation of 50 pixels (each pixel is 30m × 30 m). This procedure effectively removes deformation signals of comparable size to the filter kernel. A side effect of the high pass filtering is that atmospheric effect on the same length scale as the deformation (~10 km) is removed from the cumulative displacement map.

We then compute the structure function (Emardson et al., 2003; Lohman & Simons, 2005) by randomly selecting 1×10^6 pixel pairs from the filtered cumulative displacement map, excluding pixels within 4 km of the approximate center of deformation (to avoid residual deformation signals). The empirical structure function is defined as:

$$S(r) = \frac{1}{N}[\delta\phi(\vec{x}) - \delta\phi(\vec{x} + \vec{r})]^2 \tag{B9}$$

where r is the binned distance between pixel pairs and N is the number of pixel pairs in each bin. The empirical structure function can be fit with $S(r) = s\,[1 - exp\,(-r/\Delta)]$, where r is the variable distance between pixel pairs, s is the variance, and Δ is the characteristic distance that controls the change in variance with r. With this relationship, we can compute the covariance for each pixel with regard to a reference pixel using $C(r) = s\,[\exp(-r/\Delta)]$.

We down-sampled the cumulative displacement map using a quadtree algorithm based on a threshold variance. Following Lohman and Simons (2005), we compute the spatial covariance Σ between quadtree leaves with indices i and j using (following the notation of Anderson et al., 2019):

$$\Sigma_{i,j} = \frac{1}{n_i, n_j} \sum_{k=1}^{n_i} \sum_{l=1}^{n_j} C_{k,l}(\nabla_{i,j,k,l}) \tag{B10}$$

where n_i and n_j are the number of pixels in quadtree leaves i and j; $\nabla_{i,j,k,l}$ is the Euclidean distance between the k th and l th pixels in the quadtree leaves i and j, respectively. The resulting spatial covariance matrices for ascending and descending cumulative displacement maps are shown in Figure S2.

Appendix C: Assumption of Homogeneous Elastic Half Space

For simplicity, we assume a homogeneous elastic half space throughout this study. Here we briefly discuss the rationale to neglect effects of viscoelasticity (Dragoni & Magnanensi, 1989; Segall, 2019), poroelasticity (Liao et al., 2018), caldera bounding faults, and elastic heterogeneity due to damage (Got et al., 2017), which have been shown to be important processes in other cases.

For viscoelasticity, consider the case of a spherical magma chamber (radius R_1) surrounded by a spherical shell of Maxwell rheology (radius R_2) (Dragoni & Magnanensi, 1989; Segall, 2019), the displacement on the surface in the elastic region depends on the relaxation time:

$$t_R = \frac{3\eta(1-\nu)}{\mu(1+\nu)}\left(\frac{R_2}{R_1}\right)^3 \tag{C1}$$

where η is the viscosity of the shell, ν the Poisson's ratio, and μ the crustal shear modulus. For an order of magnitude estimate of t_R, we use a shear modulus of 3×10^9 Pa (Anderson et al., 2019), a viscosity of 5×10^{18} Pa · s (estimated for lower crust in Iceland (Sigmundsson et al., 2020)), R_2/R_1 of 2, and a Poisson's

ratio of 0.25. The estimate t_R is of order 10^2 years. Even given the elevated geothermal temperature Kīlauea, we consider t_R to be sufficiently large that viscoelastic effects are likely minor over the observation period.

For poroelasticity, the post-injection time scale is a function of both the geometry of the system and the physical properties of magma/mush (Liao et al., 2018), the later of which are especially poorly constrained. As such, exploring the time scale of poroelasticity in the context of the 2018 event is beyond the scope of this study. The effect of the cliff around the caldera bounding ring fault can be pronounced in tiltmeter data, which are sensitive to the horizontal gradient of vertical displacement, but likely minor if not undetectable in the GPS and InSAR data (Johnson et al., 2019). We also note that, models based on elastic, homogeneous half space captures co-collapse deformation outside of the caldera rim reasonably well (Segall et al., 2020), and seismicity was largely absent after the cessation of the eruption in August, 2020. These observations suggest that inelastic effects are likely minor in the post-collapse period, with possible exception of CALS, which is situated on top of the caldera block.

Appendix D: Prior Constraints on Temporal Inversion Parameters

Here we develop prior constraints on the flux model parameters (Table. 3). To account for the uncertainties in the analyses, we use the bounds deduced in this section as the limits on the uniform part of the Gaussian-tailed prior distribution. The "tail" of either end of the distribution is assigned a standard deviation equivalent to 10% the width of the uniform part.

D1. Effective Hydraulic Conductivity

Dikes, cylindrical conduits, and porous media all exhibit pressure dependent flows (Section 4). However, by assuming flow through cylindrical conduits, we can derive a range of physically plausible effective hydraulic conductivity, k, through the scaling relationships of Hagen-Poiseuille flow, assuming a linear pressure gradient:

$$k = \frac{\pi R^4}{8\eta L} \tag{D1}$$

where R is the radius of the conduit, η is magma dynamic viscosity, and L is the length of the conduit. For a thermo-dynamically stable conduit to exist, the run-away effects of magma solidification and melt-back need to be averted by balancing advective heat transport and conductive heat loss. In general, the heat transfer between a cylindrical conduit and its surroundings depends on the following dimensionless numbers: the Stefan number of the magma, the Stefan number of the surrounding crust, the Brinkman number, and the ratio between advective heat transport and conductive heat transfer, Π (Bruce & Huppert, 1989). Here we only consider the effect of Π to develop a first order estimate of plausible radii for the pathways. The bounds on the conductivities are shown not to impact the dynamic inversion results.

For $\Pi \gg 1$, advective heat transfer dominates, and the conduit will widen due to melt-back. For $\Pi \ll 1$, conductive dissipation of heat results in magma solidification and narrowing conduit (Gonnermann & Taisne, 2015). As such, the conduit radius must allow the Π to be of order 1 so that its diameter can be maintained. For a cylindrical conduit, we have the ratio as:

$$\Pi \sim \frac{D^4 \Delta p}{8 \times 16 \kappa \eta L^2} \tag{D2}$$

A factor of 8 and 16 arise from the mean conduit flow velocity and radius-diameter conversion, respectively. Assuming the dynamic viscosity of basalt is 150 Pa ·s, the magmatic over-pressure, Δp, for HMM, SC, and ERZ are ∼10 MPa, and the thermal diffusivity of basaltic lava is 5×10^{-6} m^2 s^{-1} (Hartlieb et al., 2016). For k_{SH}, L is 3 km at its maximum (given the inverted locations in the static inversion). Therefore, from Equation D2, we have $D \sim O(-1)$. For k_{HE}, k_{SE}, L is ∼ 20 km. Therefore, $D \sim O(0)$. Given that our estimated pathway diameters are of order −1 or 0, the range of radii we consider for these pathways are 0.1–1 meters

for k_{SH} and 1–10 meters for k_{HE} and k_{SE}. These two ranges of radii correspond to the effective conductivity of $O(-12) < k_{SH} < O(-8)$, $O(-9) < k_{HE}, k_{SE} < O(-5)$.

D2. Compressibility of Summit Reservoirs

The total compressibility of each magma reservoir is $\beta = \beta_m + \beta_{ch}$, where β_m is the bulk magma compressibility and β_{ch} is the magma chamber compressibility. The compressibility of bulk magma is a function of pressure and temperature, which dictates the solubility of volatile species in the magma. The compressibility of the magma chamber is a function of the bulk modulus of host rock, the geometry of the chamber, and the depth to the top of the chamber. Qualitatively, magma reservoirs with large or small aspect ratios are more compressible than those with aspect ratios close to 1 (Amoruso & Crescentini, 2009).

D2.1. Magma Chamber Compressibility

The compressibility of the magma chamber is defined as: $\beta_{ch} = \frac{1}{V}\frac{\partial V}{\partial p}$, where V is the volume of the magma chamber, and p is pressure. Analytical approximations for the pressure derivative in the above equation exist (Amoruso & Crescentini, 2009; Cervelli, 2013). However, Anderson and Segall (2011) demonstrated that, analytical approximation of the compressibility of a spheroidal magma chamber deviates significantly from the numerical solution for a depth to effective radius ratio larger than 0.75, where the effective radius is that of a volume-equivalent sphere. For robustness, we adopt the numerical emulator of Anderson et al. (2019). The numerical emulator takes as input the aspect ratio and depth to the top of a spheroid and compute the corresponding chamber compressibility, assuming a crustal shear modulus of 3×10^9 Pa (Anderson et al., 2019). To compute the chamber compressibility of HMM, we take an aspect ratio of 1.1, a depth to centroid of 1.9 km, and a volume of 3.5 km^3 (Anderson et al., 2019), which yield a chamber compressibility of 2.63×10^{-10} Pa^{-1}. For aspect ratios between 1 and 2, variation in chamber compressibility is fairly small. Assuming a volume of 2.5×10^9 km^3 for SC source (Pietruszka & Garcia, 1999), an aspect ratio of 0.18, and a depth of ∼3.5 km, we obtain a magma chamber compressibility of 8.3×10^{-10} Pa^{-1} for SC. Given fixed aspect ratio for SC, for a volume between 2.5 and 13 km^3, SC's chamber compressibility does not change significantly.

D.2.2. Magma Compressibility

Magma compressibility is defined as $\beta_m = \frac{1}{\rho_m}\frac{\partial \rho_m}{\partial p}$, where ρ_m is bulk magma density, and is a function of pressure-dependent mass concentrations of dissolved volatiles, exsolved volatiles, and phenocrysts (Anderson & Segall, 2011). We use the "degassing path" feature of VolatileCalc (Newman & Lowenstern, 2002) to compute the pressure-dependent mass concentration of dissolved H_2O and CO_2. For the upper bound of bulk magma compressibility, we assume closed-system degassing, and find the compressibility of bulk magma at SC's depth. Gerlach and Graeber (1985) estimated the mass concentration of water dissolved in chamber-equilibriated magma as 0.27 wt %, which is insensitive to depth below the top 50 m of the magma storage system. Due to magma oversaturation with CO_2 except near surface, the mass concentration of dissolved CO_2 can be computed from its solubility as a function of depth (Gerlach & Graeber, 1985). For a SC depth of ∼5 km, the magma contains 0.058 wt% of dissolved CO_2. Assuming closed system degassing, we calculate the mass concentration of exsolved volatiles in the magma chamber as the difference in that of parental magma and that of chamber-depth equilibriated magma (Gerlach & Graeber, 1985), which yields (0.3–0.27 wt % =) 0.03 wt % for H_2O and (0.65–0.058 wt % =) 0.59 wt % for CO_2. The mass fraction of exsolved volatiles with regard to bulk magma can be approximated as the sum of the calculated mass concentrations for H_2O and CO_2 because the volatiles are a very small weight percentage of the bulk magma. We input mass concentration of dissolved H_2O and CO_2 in magma equilibriated at SC's depth, magma temperature, and mass fraction of exsolved volatiles inside SC chamber into VolatileCalc to compute the dissolved volatile mass concentrations as a function of pressure (Newman & Lowenstern, 2002). We then compute bulk magma compressibility as a function of pressure through the derivative of bulk magma density with respect to pressure. SC approximate depth at ∼3.5 km corresponds to a magma-static pressure of 93 MPa. The true magmatic pressure inside SC must be at least a few MPa above the magma-static in order to drive

magma flow into the shallower HMM and ERZ. For simplicity, we take 100 MPa for pressure in SC, which yields a bulk magma compressibility of 4.24×10^{-10} Pa^{-1}. HMM's centroid is approximately 1.9 km below the surface, corresponding to a magma-static pressure of ~50 MPa. At this pressure, the degassing curve yields a compressibility of 1.46×10^{-9} Pa^{-1}.

D.2.3. Total Compressibility

The upper bound on SC total compressibility is 12.54×10^{-10} Pa^{-1}. The lower bound on SC's magma compressibility is obtained by adding the experimentally determined basaltic melt compressibility, 1×10^{-10} Pa^{-1} (Murase & McBirney, 1973), to the chamber compressibility, which yields 9.3×10^{-10} Pa^{-1}. The total compressibility of HMM is between 3.63×10^{-10} and 15.6×10^{-10} Pa^{-1}. Estimates for HMM correspond well with the 2–15 $\times 10^{-10}$ Pa^{-1} range estimated by Segall et al. (2020).

D3. Depth, Volume, Compressibility of the ERZ Reservoir

Inversion of LoS displacements from the ERZ using a Yang-Cervelli spheroid produced a centroid depth of ~2.3 km, with a semi-minor axis (sub-vertically oriented) length of ~340 m. Given that geodetic observations are most sensitive to the top, active parts of reservoirs, we use a depth range of 2–4 km below sea level for the ERZ reservoir. Because of the volume-pressure change trade-off, inversion of surface deformation does not uniquely determine the volume of the ERZ reservoir. One of the few volume estimates of reservoirs in the East Rift Zone is that of Pu'u 'Ō'ō, at $\sim 1 \times 10^7$ m^3 (Poland et al., 2014). Using this volume as the lower bound, we search for a volume between 1×10^7 m^3 and 5×10^9 m^3.

ERZ's total compressibility depends on reservoir geometry and magma volatile content. Assuming that much of the ERZ magma had undergone some degassing in the summit area, the exsolved volatile content of magma in ERZ should be lower than that of HMM. Therefore, we infer an upper bound on magma compressibility of 1.46×10^{-9} Pa^{-1}. The lower bound is that of bubble free magma, 1×10^{-10} Pa^{-1} (Murase & McBirney, 1973). For a wide range of depths and chamber aspect ratios, the chamber compressibility is of order 10^{-10} Pa^{-1}, in which case the contribution of chamber compressibility to the total compressibility is minor. Therefore, we infer a total compressibility between 1×10^{-10} and 1.5×10^{-9} Pa^{-1}. The product of ERZ volume and total compressibility is between 1×10^{-3} and 7.5 m^3 Pa^{-1}. One caveat is that, the ERZ reservoirs as a whole may behave as a dike-like feature. In that case, the chamber will contribute significantly to the total compressibility, which requires higher upper bound on the volume-compressibility product. In our preliminary search over the parameter space, the best-fit model did not approach the upper bound, so we leave the inferred priors unchanged.

D4. Initial Pressure

Prior to the caldera collapse, HMM's centroid pressure was approximately magma-static at 50 MPa, which likely is an underestimate by 1–10 MPa due to increasing magma density at depth. Anderson et al. (2019) estimated a pressure drop within HMM of ~25 MPa from the beginning to the end of May. Starting on May 29, broad collapse events took place, each associated with a co-collapse pressure increase and a post collapse gradual pressure drop. Segall et al. (2020) inferred that co-collapse pressure increase is between 1 and 3 MPa. On average, inter-collapse pressure drop may have been slightly larger than co-collapse pressure increase to produce a net deflation over three months. The cumulative co-collapse pressure change is likely a fraction of that prior to the onset of collapse, as reflected in the gradual decline of radial tilt measurements since the beginning of broad caldera collapse (Anderson et al., 2019). Assuming that the cumulative pressure drop due to the collapse events amounted to 5–10 MPa, a first order estimate of the initial pressure within HMM (at the end of collapse in August, 2018) is ~14 − 28 MPa. We estimate SC's initial pressure to be magma-static: ~93 MPa. For the dynamic inversion, we use a wide range of 60–120 MPa to account for the ambiguity of this estimation. InSAR data indicates that in early May the MERZ deflated while the LERZ inflated (Neal et al., 2019), suggesting magma transfer from the MERZ to the eruption site in the LERZ. However, given the lack of independent constraint on the ERZ's pressure in late August, we assume that ERZ's initial pressure post-collapse was close to magmastatic. With a depth to centroid between 2 and 4 km below sea level, the initial ERZ pressure is $50 - 100$ MPa.

D5. Mantle Overpressure

In Hawaii, it has been suggested that diffuse seismicity as deep as ~60 km reflects the maximum depth of melt extraction (Nicolas, 1986). Assuming an overpressure of ~5 MPa/km is generated due to the density contrast between melt and surrounding rock, p_{in} is on the order of a few hundred MPa. Due to the generality of this estimate, we set the bounds on the prior as between 100 and 300 MPa.

Data Availability Statement

GPS data are available from the UNAVCO archive (https://www.unavco.org/data/data.html). European Space Agency Sentinel 1 InSAR data are available from Alaska Satellite Facility's data repository (https://asf.alaska.edu/data-sets/derived-data-sets/insar/).

Acknowledgments
The authors thank the USGS for access to GPS data. Thanks to Dr. Kyle Anderson for helpful discussions related to the post-collapse deformation in the summit region and Prof. Howard Zebker for insights on SBAS time series analysis. The authors are grateful to the constructive comments made by the associate editor and two anonymous reviewers, which greatly improved the manuscript.

References

Agram, P. S., & Simons, M. (2015). A noise model for insar time series. *Journal of Geophysical Research Solid Earth*, *120*(4), 2752–2771. https://doi.org/10.1002/2014jb011271

Almendros, J., Chouet, B., Dawson, P., & Bond, T. (2002). Identifying elements of the plumbing system beneath kilauea volcano, Hawaii, from the source locations of very-long-period signals. *Geophysical Journal International*, *148*(2), 303–312. https://doi.org/10.1046/j.1365-246x.2002.01010.x

Amoruso, A., & Crescentini, L. (2009). Shape and volume change of pressurized ellipsoidal cavities from deformation and seismic data. *Journal of Geophysical Research*, *114*(B2). https://doi.org/10.1029/2008jb005946

Anderson, K., Johanson, I., Patrick, M. R., Gu, M., Segall, P., Poland, M., & Miklius, A. (2019). Magma reservoir failure and the onset of caldera collapse at kīlauea volcano in 2018. *Science*, *366*(6470). https://doi.org/10.1126/science.aaz1822

Anderson, K., & Segall, P. (2011). Physics-based models of ground deformation and extrusion rate at effusively erupting volcanoes. *Journal of Geophysical Research*, *116*(B7). https://doi.org/10.1029/2010jb007939

Anderson, K. R., & Poland, M. P. (2016). Bayesian estimation of magma supply, storage, and eruption rates using a multiphysical volcano model: Kīlauea Volcano, 2000-2012. *Earth and Planetary Science Letters*, *447*, 161–171. https://doi.org/10.1016/j.epsl.2016.04.029

Audet, C., & Dennis, J. E., Jr (2002). Analysis of generalized pattern searches. *SIAM Journal on Optimization*, *13*(3), 889–903. https://doi.org/10.1137/s1052623400378742

Baker, S., & Amelung, F. (2012). Top-down inflation and deflation at the summit of kīlauea volcano, Hawai 'i observed with insar. *Journal of Geophysical Research*, *117*(B12). https://doi.org/10.1029/2011jb009123

Baker, S., & Amelung, F. (2015). Pressurized magma reservoir within the east rift zone of Kīlauea Volcano, Hawai'i: Evidence for relaxed stress changes from the 1975 Kalapana earthquake. *Geophysical Research Letters*, *42*(6), 1758–1765. https://doi.org/10.1002/2015gl063161

Bato, M. G., Pinel, V., Yan, Y., Jouanne, F., & Vandemeulebrouck, J. (2018). Possible deep connection between volcanic systems evidenced by sequential assimilation of geodetic data. *Scientific Reports*, *8*(1), 1–13. https://doi.org/10.1038/s41598-018-29811-x

Berardino, P., Fornaro, G., Lanari, R., & Sansosti, E. (2002). A new algorithm for surface deformation monitoring based on small baseline differential sar interferograms. *IEEE Transactions on Geoscience and Remote Sensing*, *40*(11), 2375–2383. https://doi.org/10.1109/tgrs.2002.803792

Bruce, P. M., & Huppert, H. E. (1989). Thermal control of basaltic fissure eruptions. *Nature*, *342*(6250), 665–667. https://doi.org/10.1038/342665a0

Cervelli, P. (2013). Analytical expressions for deformation from an arbitrarily oriented spheroid in a half-space.

Cervelli, P., & Miklius, A. (2003). The shallow magmatic system of kilauea volcano. *U. S. Geological Survey Professional Paper*, *1676*, 149–163.

Dawson, P. B., Chouet, B. A., Okubo, P. G., Villaseñor, A., & Benz, H. M. (1999). Three-dimensional velocity structure of the kilauea caldera, Hawaii. *Geophysical Research Letters*, *26*(18), 2805–2808. https://doi.org/10.1029/1999gl005379

Delaney, P. T., & Gartner, A. E. (1997). Physical processes of shallow mafic dike emplacement near the san rafael swell, Utah. *Geological Society of America Bulletin*, *109*(9), 1177–1192. https://doi.org/10.1130/0016-7606(1997)109<1177:pposmd>2.3.co;2

Dieterich, J. H., & Decker, R. W. (1975). Finite element modeling of surface deformation associated with volcanism. *Journal of Geophysical Research*, *80*(29), 4094–4102. https://doi.org/10.1029/jb080i029p04094

Dietterich, H. R., Diefenbach, A. K., Soule, S. A., Zoeller, M. H., Patrick, M. P., Major, J. J., & Lundgren, P. R. (2021). Lava effusion rate evolution and erupted volume during the 2018 kīlauea lower east rift zone eruption. *Bulletin of Volcanology*, *83*(4), 1–18. https://doi.org/10.1007/s00445-021-01443-6

Diez, M., Connor, C., Connor, L., & Savov, I. (2005). Magma dynamics and conduit growth mechanisms inferred from exposed volcano conduits at the san rafael subvolcanic field, utah. *AGUFM*.

Dragoni, M., & Magnanensi, C. (1989). Displacement and stress produced by a pressurized, spherical magma chamber, surrounded by a viscoelastic shell. *Physics of the Earth and Planetary Interiors*, *56*(3–4), 316–328. https://doi.org/10.1016/0031-9201(89)90166-0

Dvorak, J., Okamura, A., & Dieterich, J. H. (1983). Analysis of surface deformation data, kilauea volcano, hawaii: October 1966 to september 1970. *Journal of Geophysical Research*, *88*(B11), 9295–9304. https://doi.org/10.1029/jb088ib11p09295

Dzurisin, D., & Poland, M. P. (2018). Magma supply to kīlauea volcano, hawai 'i, from inception to now: Historical perspective, current state of knowledge, and future challenges. *Field volcanology: A tribute to the distinguished career of Don Swanson, Geological Society of America Special Paper*, *538*, 275–295.

Eaton, J. P. (1962). Crustal structure and volcanism in hawaii. *The Crust of the Pacific Basin*, *6*, 13–29.

Emardson, T., Simons, M., & Webb, F. (2003). Neutral atmospheric delay in interferometric synthetic aperture radar applications: Statistical description and mitigation. *Journal of Geophysical Research: Solid Earth*, *108*(B5). https://doi.org/10.1029/2002jb001781

Fialko, Y., Simons, M., & Agnew, D. (2001). The complete (3-D) surface displacement field in the epicentral area of the 1999MW7.1 Hector Mine Earthquake, California, from space geodetic observations. *Geophysical Research Letters*, *28*(16), 3063–3066. https://doi.org/10.1029/2001gl013174

Fiske, R. S., & Kinoshita, W. T. (1969). Inflation of kilauea volcano prior to its 1967-1968 eruption. *Science*, *165*(3891), 341–349. https://doi.org/10.1126/science.165.3891.341

Gansecki, C., Lee, R. L., Shea, T., Lundblad, S. P., Hon, K., & Parcheta, C. (2019). The tangled tale of kīlauea's 2018 eruption as told by geochemical monitoring. *Science*, *366*(6470). https://doi.org/10.1126/science.aaz0147

Gerlach, T. M., & Graeber, E. J. (1985). Volatile budget of kilauea volcano. *Nature*, *313*(6000), 273–277. https://doi.org/10.1038/313273a0

Gonnermann, H., & Taisne, B. (2015). Magma transport in dikes. In *The encyclopedia of volcanoes* (pp. 215–224). Elsevier. https://doi.org/10.1016/b978-0-12-385938-9.00010-9

Got, J.-L., Carrier, A., Marsan, D., Jouanne, F., Vogfjörd, K., & Villemin, T. (2017). An analysis of the nonlinear magma-edifice coupling at Grimsvötn volcano (Iceland). *Journal of Geophysical Research Solid Earth*, *122*(2), 826–843. https://doi.org/10.1002/2016jb012905

Guarnieri, A. M., & Tebaldini, S. (2008). On the exploitation of target statistics for sar interferometry applications. *IEEE Transactions on Geoscience and Remote Sensing*, *46*(11), 3436–3443. https://doi.org/10.1109/tgrs.2008.2001756

Gutmann, H.-M. (2001). A radial basis function method for global optimization. *Journal of Global Optimization*, *19*(3), 201–227. https://doi.org/10.1023/a:1011255519438

Hartlieb, P., Toifl, M., Kuchar, F., Meisels, R., & Antretter, T. (2016). Thermo-physical properties of selected hard rocks and their relation to microwave-assisted comminution. *Minerals Engineering*, *91*, 34–41. https://doi.org/10.1016/j.mineng.2015.11.008

Johnson, J. H., Poland, M. P., Anderson, K. R., & Biggs, J. (2019). A Cautionary Tale of Topography and Tilt from Kīlauea Caldera. *Geophysical Research Letters*, *46*(8), 4221–4229. https://doi.org/10.1029/2018gl081757

Jolivet, R., Agram, P. S., Lin, N. Y., Simons, M., Doin, M. P., Peltzer, G., & Li, Z. (2014). Improving insar geodesy using global atmospheric models. *Journal of Geophysical Research Solid Earth*, *119*(3), 2324–2341. https://doi.org/10.1002/2013jb010588

Keating, G. N., Valentine, G. A., Krier, D. J., & Perry, F. V. (2008). Shallow plumbing systems for small-volume basaltic volcanoes. *Bulletin of Volcanology*, *70*(5), 563–582. https://doi.org/10.1007/s00445-007-0154-1

Koyanagi, R., Unger, J., Endo, E., & Okamura, A. (1976). Shallow earthquakes associated with inflation episodes at the summit of kilauea volcano, hawaii. *Bulletin of Volcanology*, *39*, 621–631

Le Mével, H., Gregg, P. M., & Feigl, K. L. (2016). Magma injection into a long-lived reservoir to explain geodetically measured uplift: Application to the 2007-2014 unrest episode at Laguna del Maule volcanic field, Chile. *Journal of Geophysical Research Solid Earth*, *121*(8), 6092–6108. https://doi.org/10.1002/2016jb013066

Liang, C., Agram, P., Simons, M., & Fielding, E. J. (2019). Ionospheric correction of insar time series analysis of c-band sentinel-1 tops data. *IEEE Transactions on Geoscience and Remote Sensing*, *57*(9), 6755–6773. https://doi.org/10.1109/tgrs.2019.2908494

Liao, Y., Soule, S. A., & Jones, M. (2018). On the mechanical effects of poroelastic crystal mush in classical magma chamber models. *Journal of Geophysical Research Solid Earth*, *123*(11), 9376–9406. https://doi.org/10.1029/2018jb015985

Lin, Y.-n. N., Simons, M., Hetland, E. A., Muse, P., & DiCaprio, C. (2010). A multiscale approach to estimating topographically correlated propagation delays in radar interferograms. *Geochemistry, Geophysics, Geosystems*, *11*(9). https://doi.org/10.1029/2010gc003228

Lohman, R. B., & Simons, M. (2005). Some thoughts on the use of insar data to constrain models of surface deformation: Noise structure and data downsampling. *Geochemistry, Geophysics, Geosystems*, *6*(1). https://doi.org/10.1029/2004gc000841

Lundgren, P., Poland, M., Miklius, A., Orr, T., Yun, S.-H., Fielding, E., et al. (2013). Evolution of dike opening during the March 2011 Kamoamoa fissure eruption, Kīlauea Volcano, Hawai`i. *Journal of Geophysical Research Solid Earth*, *118*(3), 897–914. https://doi.org/10.1002/jgrb.50108

Mastin, L. G., & Ghiorso, M. S. (2000). *A numerical program for steady-state flow of magma-gas mixtures through vertical eruptive conduits*. (Tech. Rep.). Department of the Interior. https://doi.org/10.3133/ofr00209

Mastin, L. G., Roeloffs, E., Beeler, N. M., & Quick, J. E. (2008). *Constraints on the size, overpressure, and volatile content of the mount st. helens magma system from geodetic and dome-growth measurements during the 2004-2006+ eruption* (Tech. Rep.). US Geological Survey

Miklius, A., Cervelli, P., Sako, M., Lisowski, M., Owen, S., Segal, P., & Brooks, B. (2005). Global positioning system measurements on the island of hawai'i: 1997 through 2004. *US Geological Survey Open File Report*, *1425*, 1–48.

Montagna, C. P., & Gonnermann, H. M. (2013). Magma flow between summit and Pu'u 'Ō'ō at Kīlauea Volcano, Hawai'i. *Geochemistry, Geophysics, Geosystems*, *14*(7), 2232–2246. https://doi.org/10.1002/ggge.20145

Montgomery-Brown, E. K., Sinnett, D., Poland, M., Segall, P., Orr, T., Zebker, H., & Miklius, A. (2010). Geodetic evidence for en echelon dike emplacement and concurrent slow slip during the June 2007 intrusion and eruption at kīlauea volcano, hawaii. *Journal of Geophysical Research: Solid Earth*, *115*(B7). https://doi.org/10.1029/2009jb006658

Murase, T., & McBirney, A. R. (1973). Properties of some common igneous rocks and their melts at high temperatures. *The Geological Society of America Bulletin*, *84*(11), 3563–3592. https://doi.org/10.1130/0016-7606(1973)84<3563:poscir>2.0.co;2

Neal, C. A., Brantley, S. R., Antolik, L., Babb, J. L., Burgess, M., Calles, K., et al. (2019). The 2018 rift eruption and summit collapse of Kīlauea Volcano. *Science*, *363*(6425), 367–374. https://doi.org/10.1126/science.aav7046

Newman, S., & Lowenstern, J. B. (2002). VolatileCalc: A silicate melt-H2O-CO2 solution model written in Visual Basic for excel. *Computers & Geosciences*, *28*(5), 597–604. https://doi.org/10.1016/s0098-3004(01)00081-4

Nicolas, A. (1986). A melt extraction model based on structural studies in mantle peridotites. *Journal of Petrology*, *27*(4), 999–1022. https://doi.org/10.1093/petrology/27.4.999

Ohminato, T., Chouet, B. A., Dawson, P., & Kedar, S. (1998). Waveform inversion of very long period impulsive signals associated with magmatic injection beneath kilauea volcano, hawaii. *Journal of Geophysical Research*, *103*(B10), 23839–23862. https://doi.org/10.1029/98jb01122

Owen, S., Segall, P., Lisowski, M., Miklius, A., Murray, M., Bevis, M., & Foster, J. (2000). January 30, 1997 eruptive event on kilauea volcano, hawaii, as monitored by continuous gps. *Geophysical Research Letters*, *27*(17), 2757–2760. https://doi.org/10.1029/1999gl008454

Papale, P., Neri, A., & Macedonio, G. (1998). The role of magma composition and water content in explosive eruptions: 1. Conduit ascent dynamics. *Journal of Volcanology and Geothermal Research*, *87*(1–4), 75–93. https://doi.org/10.1016/s0377-0273(98)00101-2

Patrick, M., Orr, T., Anderson, K., & Swanson, D. (2019). Eruptions in sync: Improved constraints on Kīlauea Volcano's hydraulic connection. *Earth and Planetary Science Letters*, *507*, 50–61. https://doi.org/10.1016/j.epsl.2018.11.030

Patrick, M. R., Anderson, K. R., Poland, M. P., Orr, T. R., & Swanson, D. A. (2015). Lava lake level as a gauge of magma reservoir pressure and eruptive hazard. *Geology*, *43*(9), 831–834. https://doi.org/10.1130/g36896.1

Pietruszka, A. J., & Garcia, M. O. (1999). The size and shape of kilauea volcano's summit magma storage reservoir: A geochemical probe. *Earth and Planetary Science Letters*, *167*(3–4), 311–320. https://doi.org/10.1016/s0012-821x(99)00036-9

Poland, M. P., Miklius, A., & Montgomery-Brown, E. K. (2014). Magma supply, storage, and transport at shield-stage Hawaiian volcanoes. *Charact. Hawaii. Volcanoes*, *179*(1801), 179–234. https://doi.org/10.3133/pp18015

Poland, M. P., Peltier, A., Bonforte, A., & Puglisi, G. (2017). The spectrum of persistent volcanic flank instability: A review and proposed framework based on Kīlauea, Piton de la Fournaise, and Etna. *Journal of Volcanology and Geothermal Research*, *339*, 63–80. https://doi.org/10.1016/j.jvolgeores.2017.05.004

Poland, M. P., Sutton, A. J., & Gerlach, T. M. (2009). Magma degassing triggered by static decompression at kīlauea volcano, hawai 'i. *Geophysical Research Letters*, *36*(16). https://doi.org/10.1029/2009gl039214

Pollard, D., & Delaney, P. (1978). Basaltic subvolcanic conduits near shiprock, new-mexico-dike propagation and dilation. In *Transactions-american geophysical union* (Vol. 59, pp. 1212–1213).

Reverso, T., Vandemeulebrouck, J., Jouanne, F., Pinel, V., Villemin, T., Sturkell, E., & Bascou, P. (2014). A two-magma chamber model as a source of deformation at Grímsvötn Volcano, Iceland. *Journal of Geophysical Research Solid Earth*, *119*(6), 4666–4683. https://doi.org/10.1002/2013jb010569

Ryan, M. P. (1988). The mechanics and three-dimensional internal structure of active magmatic systems: Kilauea volcano, hawaii. *Journal of Geophysical Research*, *93*(B5), 4213–4248. https://doi.org/10.1029/jb093ib05p04213

Segall, P. (2019). Magma chambers: What we can, and cannot, learn from volcano geodesy. *Philosophical Transactions of the Royal Society A*, *377*(2139), 20180158. https://doi.org/10.1098/rsta.2018.0158

Segall, P., Anderson, K. R., Pulvirenti, F., Wang, T., & Johanson, I. (2020). Caldera collapse geometry revealed by near-field gps displacements at kīlauea volcano in 2018. *Geophysical Research Letters*, *47*(15), e2020GL088867. https://doi.org/10.1029/2020gl088867

Segall, P., Cervelli, P., Owen, S., Lisowski, M., & Miklius, A. (2001). Constraints on dike propagation from continuous gps measurements. *Journal of Geophysical Research*, *106*(B9), 19301–19317. https://doi.org/10.1029/2001jb000229

Sigmundsson, F., Pinel, V., Grapenthin, R., Hooper, A., Halldórsson, S. A., Einarsson, P., et al. (2020). Unexpected large eruptions from buoyant magma bodies within viscoelastic crust. *Nature Communications*, *11*(1), 1–11. https://doi.org/10.1038/s41467-020-16054-6

Simons, M., Fialko, Y., & Rivera, L. (2002). Coseismic deformation from the 1999 Mw 7.1 Hector Mine, California, Earthquake as inferred from InSAR and GPS observations. *Bulletin of the Seismological Society of America*, *92*(4), 1390–1402. https://doi.org/10.1785/0120000933

Tepp, G., Hotovec-Ellis, A., Shiro, B., Johanson, I., Thelen, W., & Haney, M. M. (2020). Seismic and geodetic progression of the 2018 summit caldera collapse of kīlauea volcano. *Earth and Planetary Science Letters*, *540*, 116250. https://doi.org/10.1016/j.epsl.2020.116250

Tough, J., Blacknell, D., & Quegan, S. (1995). A statistical description of polarimetric and interferometric synthetic aperture radar data. *Proceedings of the Royal Society of London*, *449*(1937), 567–589.

Wieser, P. E., Lamadrid, H., Maclennan, J., Edmonds, M., Matthews, S., Iacovino, K., et al. (2020). Reconstructing magma storage depths for the 2018 kılauean eruption from melt inclusion co2 contents: The importance of vapor bubbles. *Geochemistry, Geophysics, Geosystems*, e2020GC009364. https://doi.org/10.46427/gold2020.2860

Wilson, L., & Head, J. W., III. (1981). Ascent and eruption of basaltic magma on the earth and moon. *Journal of Geophysical Research*, *86*(B4), 2971–3001. https://doi.org/10.1029/jb086ib04p02971

Yang, X.-M., Davis, P. M., & Dieterich, J. H. (1988). Deformation from inflation of a dipping finite prolate spheroid in an elastic half-space as a model for volcanic stressing. *Journal of Geophysical Research*, *93*(B5), 4249–4257. https://doi.org/10.1029/jb093ib05p04249

Zebker, H. A. (2017). User-friendly insar data products: Fast and simple timeseries processing. *IEEE Geoscience and Remote Sensing Letters*, *14*(11), 2122–2126. https://doi.org/10.1109/lgrs.2017.2753580

Zheng, Y., & Zebker, H. A. (2017). Phase correction of single-look complex radar images for user-friendly efficient interferogram formation. *IEEE Journal of Selected Topics Earth Observations Remote Sensing*, *10*(6), 2694–2701. https://doi.org/10.1109/jstars.2017.2697861

Zheng, Y., Zebker, H., & Michaelides, R. (2021). A new decorrelation phase covariance model for noise reduction in unwrapped interferometric phase stacks. *IEEE Transactions on Geoscience and Remote Sensing*.